Exchange Stiffness in Thin-Film Cobalt Alloys

by

Charles Eyrich

B.Sc., Dalhousie University, 2010

THESIS SUBMITTED IN PARTIAL FULFILLMENT

OF THE REQUIREMENTS FOR THE DEGREE OF

MASTER OF SCIENCE

IN THE

DEPARTMENT OF PHYSICS

FACULTY OF SCIENCE

SIMON FRASER UNIVERSITY

Fall 2012

APPROVAL

Name: Charles Eyrich

Degree: Master of Science

Title of Thesis: Exchange Stiffness in Thin-Film Cobalt Alloys

Examining Committee: Dr. J. Steven Dodge
Associate Professor (Chair)

Dr. Erol Girt, Senior Supervisor
Associate Professor

Dr. Bret Heinrich, Co-Supervisor
Professor Emeritus

Dr. Simon Watkins, Supervisor
Associate Professor

Dr. David Broun, Internal Examiner
Associate Professor

Date Approved: November 29th, 2012

Partial Copyright Licence

Abstract

The exchange stiffness, A_{ex}, is one of the key parameters controlling magnetization reversal in magnetic materials but is very difficult to measure, especially in thin films. We developed a new technique for measuring the exchange stiffness of a magnetic material based on the formation of a spin spiral within two antiferromagnetically coupled ferromagnetic films [1]. Using this method, I was able to measure the exchange stiffness of thin film Co alloyed with Cr, Fe, Ni, Pd, Pt and Ru. The results of this work showed that the rate at which a substituent element reduces the exchange stiffness is not directly related to its effect on the magnetization of the alloy. These measured trends have been understood by combining measurements of element specific magnetic moments obtained using X-ray magnetic circular dichroism (XMCD) and material specific modeling based on density functional theory (DFT) within the local density approximation (LDA). The experimental results also hint at significant reduction of the exchange stiffness at the interface that can account for the difference between our results and those obtained on bulk materials.

I dedicate this thesis to Furious George

Acknowledgments

I would like to thank several groups of people that contributed to this completed thesis. First, to my family, without whom I would likely not have become a graduate student and would not be the person I am today. Secondly, I would like to thank my girlfriend Troë for pushing me to get this finished so I can move on to the next part of my life. Thirdly I would like to thank all members of Furious George who never gave up on me during my numerous injuries. Without their assistance I would not be playing the sport I love that helps keep me sane.

I would also like to thank Wendell, Ken, Monika, Farnaz, Eric, Duncan, Bret, and Erol for helping out with various parts of this thesis. Friendship is worth so much, and consequently I would also like to extend a very warm thank you to Natalie, Sonia, Louise, Paul, and the many others who have made my life worth living.

While I have space I should also thank my physiotherapist David Terlichter and surgeon Dr. Pierre Guy for helping me stand strong on my knee again.

Contents

List of Tables

List of Figures

Chapter 1

Introduction

According to Eric Schmidt, the CEO of Google, 5 exabytes, that is 5×10^{18} bytes, of information are created every two days and this has to be stored somewhere. In this technological revolution there is an ever increasing demand for more hard drives with more storage capacity. Over the last several decades information storage has shown some remarkable progress with hard drive capacity doubling almost every 12-18 months [2, 3]. Since the first hard drives were produced in 1950, the storage capacity per disk has increased by factor of 150,000 [2], a number which is all the more impressive when one realizes that current hard drives have a 3.5" diameter disc, whereas, in the 1950s, a hard drive consisted of around fifty 24" diameter discs. Taken together, the recording density has increased by a factor of 65×10^6.

The increase in the areal density has been due largely to changes in the three main magnetic components of hard drives: 1) the recording media, 2) the write element of the magnetic head, and 3) the read element of the magnetic head [2–4]. However, new technologies are going to be required if information storage is going to continue to increase at anything close to this historical rate [2–5].

As shown in Figure 1.1, the write head is made from an monopole electromagnet with a high magnetization saturation, M_s, material acting as a core [4]. As the write head passes over the disc, the magnetic field produced by the write head sets the magnetization direction of the magnetic grains in the disc, thereby storing information in the magnetic state of the grain. The maximum write field is limited by the M_s, of the materials in the write head monopole. Write heads currently use an $Fe_{65}Co_{35}$ alloy in the core of the monopole

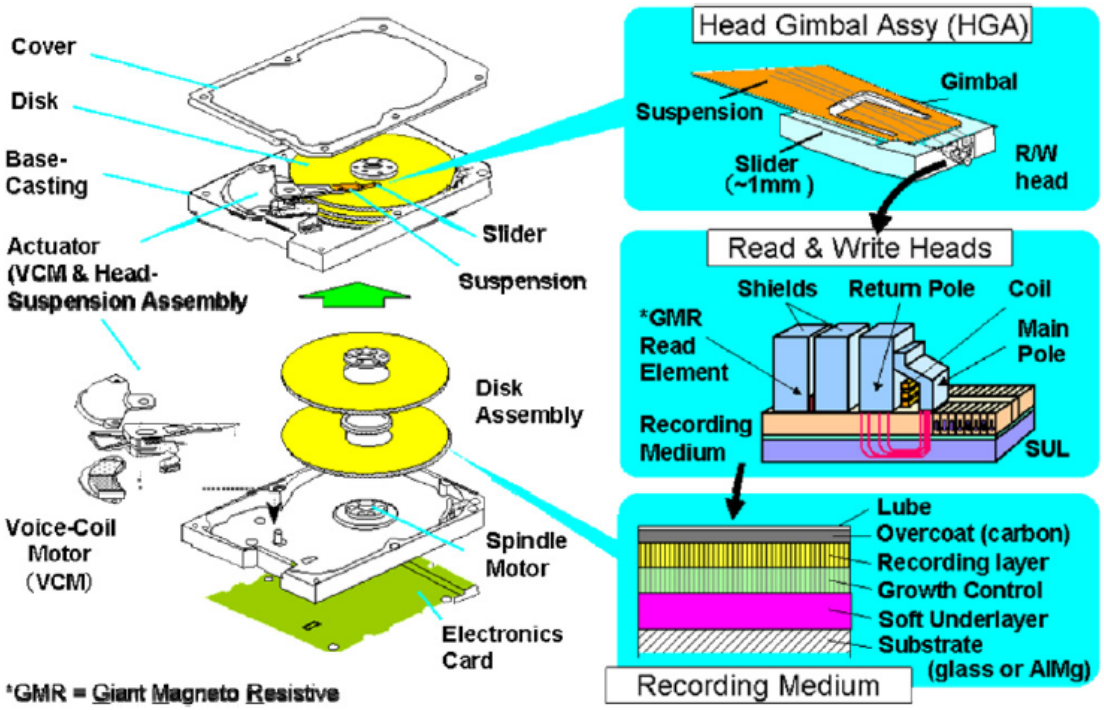

Figure 1.1: Hard drives consist of two major parts: a recording head and magnetic media. The recording head consists of a write head that produces a large magnetic field to reverse the magnetization in the media, and a read head which measures the magnetization of media. The read head is a GMR sensor that is made from a pinned and free magnetic layers separated by a non-magnetic spacer layer. The magnetization direction of the free layer reacts to the magnetic field produced by the media. The relative orientation of the magnetization of the free and pinned layer determines the resistance of the sensor, thereby indicating the magnetization state of the media. Reprinted from Wood [4]; used with permission from Elsevier.

electromagnet to produce magnetic fields up to 2.4 T, which is equal to $4\pi M_s$ of this alloy [6].

The read head is made of a giant magnetoresistance (GMR), or more recently a tunneling magnetoresistance (TMR), sensor [2–4]. Magnetoresistance (MR) is the phenomenon where the magnetization of a material affects its electrical resistance. GMR and TMR effects are present in multilayer structures containing two ferromagnetic layers separated by

a non-magnetic spacer layer [7–9]. GMR is present in structures with a conductive spacer layer while TMR is observed in structures with an insulating spacer layer. The resistance of this tri-layer structure depends on the relative orientation of the magnetization of the ferromagnetic layers. The resistance is smallest when the magnetizations are parallel and largest when they are antiparallel [10].

The development of GMR and TMR sensors enabled dramatic improvements in recording density. For the discovery of GMR, Albert Fert and Peter Grünberg were awarded the Nobel Prize for physics in 2007 [10]. The two magnetic layers in a GMR sensor are called the pinned and free layers [11]. The magnetization of the pinned layer is fixed perpendicular to the surface of the disc. A small external magnetic field is applied to align the magnetization direction of the free layer perpendicular to the magnetization direction of the pinned layer, and therefore parallel to the surface. This is done to maximise the sensitivity of the sensor. The magnetic moments in the free layer interacts with the magnetic fields from the media. This causes a change in the direction of the magnetization of the free layer, and consequently a change in the relative orientation of the magnetic moments in the free and pinned layers. Since the resistance depends on the relative orientation of magnetic moments in the free and pinned layers, measuring the resistivity across this sensor indirectly indicates the magnetization direction of the free layer, and therefore the strength and direction of the magnetic field produced by magnetic grains in the media.

Substantial improvements have also been made in the media to improve performance [2–5, 12]. Magnetic media stores information in the magnetization direction of a small area of the disc containing several magnetic grains. Reducing the grain size increases the recording density because the magnetic transition between two bits, which is related to the grain size, decreases. Also the signal-to-noise ratio (SNR) is proportional to the square root of the number of grains per bit [11–14]. So with smaller grains, more bits can be fit into the same area without negatively impacting the SNR.

While smaller grains are preferable they are less magnetically stable. The magnetic energy of a grain is KV where K is the magnetic anisotropy constant and V is the volume of the grain. In order for the magnetization to be considered stable, the magnetic energy has to be 40 times larger than the thermal energy, k_BT, where k_B is Boltzmann's constant and T is the temperature [12, 14, 15]. For this reason, smaller grains must have larger anisotropy constants such that $KV/k_BT > 40$. The field required to reverse the magnetization of a grain

with an anisotropy constant K is proportional to $\frac{K}{M_s}$. One way to improve the recording density is to match increases the field produced by the write head with high anisotropy materials for the media. This is unlikely, however, because it would require the invention of easily manufactured materials with larger M_s than that of FeCo at hard drive operating temperatures. Another option is to develop new techniques for magnetization reversal of the grains. Two of the most researched methods for modifying magnetic reversal involve exchange coupled media and heat-assisted magnetic recording (HAMR) [14, 16–20].

HAMR systems use targeted heating to assist in writing [14, 16]. K drops with temperature, which allows for magnetization reversal of grains with arbitrarily large K at existing head fields at higher temperatures. Upon cooling, the anisotropy will return to its initial value thereby maintaining thermal stability of the grain. Recently, Seagate Technology demonstrated that HAMR can be used to record densities of 1Tbit per square inch, the largest ever for magnetic media [21].

Another option is to construct the magnetic recording layer out of 2 or more magnetic layers with a grading of anisotropies, in so called exchange coupled composite (ECC) media as shown in Figure 1.2 [17–20, 22].

ECC media, like HAMR media, should be writable with current head fields. The reversal dynamics in exchange coupled media have been studied quite thoroughly by Dieter Suess [17–19], an example of which is shown in Figure 1.3. The small anisotropy layers begin to rotate first under the external field. Due to the strong direct exchange coupling in the magnetic grains the reversal of the soft layers creates an additional torque that helps magnetization reversal of the higher anisotropy layers. The coercivity of ECC media can be up to 10 times lower than that of single recording layer media with the same magnetic energy of the grains [17–20, 22].

The largest obstacle to the production of exchange-coupled media lies in finding magnetic materials with the required magnetocrystalline anisotropy K, saturation magnetization M_s, and exchange stiffness A_{ex}. K and M_s are easy to measure. However, A_{ex} is very difficult to measure, especially in thin films. A_{ex} describes the strength of the direct exchange interaction between magnetic moments in a ferromagnet. Thus, it controls non-uniform magnetization reversal of ECC media.

In 2010, Girt et al. [1] proposed a new method for measuring the exchange stiffness in thin films using micromagnetic simulations. Typically the exchange stiffness of a material

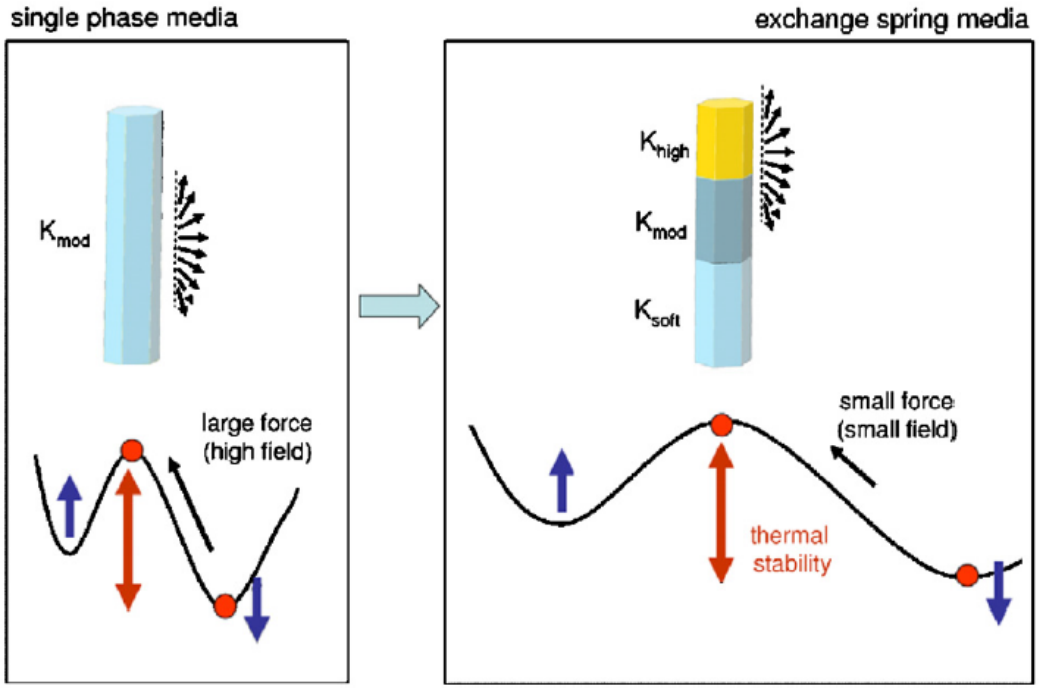

Figure 1.2: Exchange spring media, shown on the right, consist of at least two magnetic layers with graded anisotropies as opposed to the conventional single recording layer media, on the left. Both structures can have the same thermal stability, but ECC media reverse at much lower applied fields. K_{high}, K_{mod}, and K_{low} identify regions of high, moderate and low magnetic anisotropy in the grain. Reprinted from Suess et al. [19]; used with permission from Elsevier.

is measured by exciting magnon modes using ferromagnetic resonance (FMR), Brillouin Light Scattering (BLS), or neutron scattering (NS). FMR, BLS, and NS measure A_{ex} from the dispersion curve of spin waves in the ferromagnet. The energy required to excited a spin wave is given by [23, 24]:

$$E_{magnon} = \hbar\omega = \hbar\gamma\left[\left(H_0 + \frac{2A_{ex}}{M_s}Q^2\right)\left(H_0 + \frac{2A_{ex}}{M_s}Q^2 + 4\pi M_s\right)\right]^{\frac{1}{2}}, \tag{1.1}$$

where: γ is the gyromagnetic ratio, H_0 is the applied field, $Q = \frac{n\pi}{L}$ is the magnon wave vector, L is the sample thickness, and $n = 0,\ 1,\ 2,\ 3\ \ldots$ indicates the homogenous, first, second, third, etc. modes. This energy is inveresly related to the film thickness. At zero

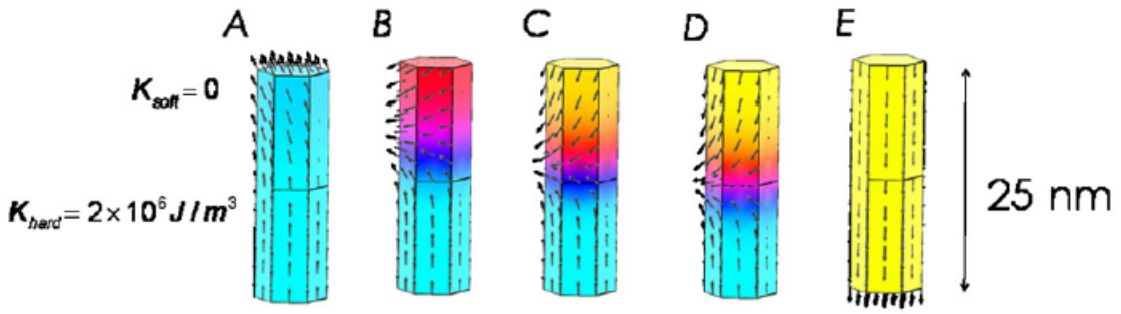

Figure 1.3: Simulation performed by Suess et al. [19] on a two layer ECC system demonstrating the non-uniform reversal of the media. The figure shows the direction of the magnetic moments during reversal. A is the initial state and E is the reversed state. The soft layer on top rotates first and through the exchange interaction, aids in rotating the magnetization of the bottom layer. Reprinted from Suess et al. [19]; used with permission from Elsevier.

field, the frequency, f, of the first order magnon mode is 580 GHz as calculated from Equation 1.1, with A_{ex}= 1.5×10^{-6} erg/cm, M_s=1250 emu/cm^3, $\gamma = \frac{g\mu_B}{\hbar}$, g is the electron g-factor, μ_B is the Bohr magneton, and $L = 100$ Å. This frequency cannot be generated with FMR and the free spectral range of the interferometers used in BLS cannot resolve such large frequencies. NS measurements may only be done in reflectivity mode due to the large penetration depth of neutrons. For these reasons these techniques are usually used for measuring the exchange stiffness of films exceeding 300 Å in thickness [24–26]. Micromagnetic simulations are not limited by the thickness of the magnetic layers. In this study, I will show that this method may be used to measure the exchange stiffness of films down to 24 Å in thickness and perhaps further.

Co is the only 3d elemental ferromagnet with lower than cubic bulk symmetry. Therefore, it has a much larger magnetocrystalline anisotropy than Fe or Ni, the other 3d ferromagnets. Moreover, high anisotropy Co alloys can be fabricated at room temperature. For these reasons, current recording media are made primarily from Co alloys. Hexagonal Co has among the highest A_{ex} of the metallic ferromagnets. Measurements of A_{ex} indicate a large descrepency in the values: $1.8 \pm .3 \times 10^{-11}$ J/m from BLS [24], $2.7 \pm .1 \times 10^{-11}$ J/m from neutron scattering [27], and 2.1×10^{-11} J/m from FMR studies [28]. As already mentioned, all these measurements were done on thick films and may not be

accurate for the thin film structures used in hard drives.

In this thesis, it will be shown that the exchange stiffness of a ferromagnetic layer can be determined by fitting M(H) curves of two ferromagnetic layers antiferromagnetically coupled across a non-magnetic Ru spacer layer with a simple micromagnetic model. The thesis will start with an explanation of the methods used to deposit the structures, followed by the techniques used to measure the structural and magnetic properties of the films. The next section covers the micromagnetic models used to simulate the tri-layer structure. The penultimate chapter presents the results of these experiments. The exchange stiffness of Co alloyed with Cr, Fe, Ni, Pd, Pt, and Ru is presented along with measurements of the thickness dependence of the exchange stiffness of Co. The work is summarized in the last chapter.

Chapter 2

Experimental Procedure

This chapter addresses the deposition and measurement techniques used in this thesis. The first section discusses the sputtering deposition used in fabricating the multilayer structures. The next section explains the X-ray techniques used to determine the structural properties of the films. The magnetometry was performed using both a Superconducing Quantum Interference Device (SQUID) and Vibrating Sample Magnetometer (VSM). The principles behind both of these experiments are explained. The final section is a short explanation of X-ray Magnetic Circular Dichroism (XMCD), an experimental technique that was used to measure the magnetic moments of individual elements in the alloys. While I did not perform the XMCD measurements, the results of these measurements aid in understanding the observed trends of A_{ex}.

2.1 Sample Deposition

The magnetic films studied for this thesis were deposited at room temperature onto Si (100) substrates using Direct Current (DC) and Radio Frequency (RF) sputtering techniques. (100) refers to the atomic plane orientation aligned with the substrate surface. Prior to the deposition, the substrates were cleaned in heated hexane and methanol baths to remove organics from the surface and rinsed in de-ionized water. All three processes were aided by ultrasonic agitation. Upon removal from de-ionized water the wafers were blown dry with N_2 gas.

Sputtering deposition works by colliding high kinetic energy gas particles with a target

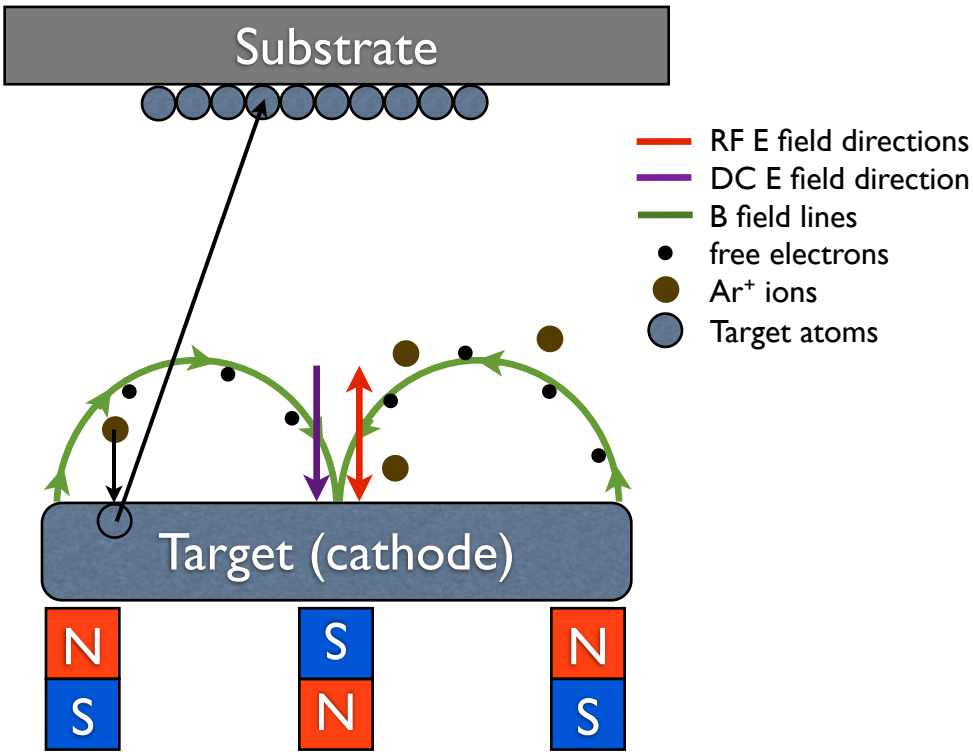

Figure 2.1: Sputtering requires the transfer of kinetic energy from the plasma to atoms in the target in order to eject target atoms towards the substrate. Magnets below the target trap electrons in helical orbits around the magnetic field lines. These electrons ionize Ar atoms that are then accelerated by the electric field towards the cathode target, which upon impact, free both the traget atoms that get deposited on the substrate, and electrons that get trapped in the magnetic field to continue the process. This schematic only shows one out of the six sputtering guns in the deposition chamber. In the case of DC sputtering the target always acts as a cathode to attract Ar^+ ions.As such, the E field lines point toward the target and are perpendicular to the target surface. In case of RF sputtering, the potential of target varies periodically from positive to attract electrons and negative to attract Ar^+ ions. In this case, the E field lines constantly change direction but remain perpendicular to the target surface. The direction of the field, in both cases, is shown in the figure. The E field exists throughout the figure, however I am only showing a few lines that are important in accelerating the Ar^+ ions towards the target.

material in order to eject atoms from the target onto a substrate as shown in Figure 2.1. The kinetic energy of the gas atoms comes from ionizing the Ar gas subjecting it to a large electric field produced by applying a large negative voltage to the target. The plasma formed during the sputtering process consists of Ar^+ ions produced by collisions between neutral Ar atoms and electrons trapped by the magnetic field above the target which have been accelerated in the electric field. This magnetic field is produced by a ring of magnets below the target as shown in Figure 2.1. Ar^+ ions are then accelerated towards the target by applying a negative voltage to the target. Upon impact, the ions eject both target atoms and electrons. Many of these electrons get trapped by the magnetic field and continue the ionization process. Figure 2.1 only shows one of the six sputtering guns that are equidistant from the substrate. Each sputter gun was used for a different material.

DC sputtering only works with targets made from conductive materials. The reason being that the target must serve as the cathode in order to attract the Ar^+ ions during the sputtering process. However, during collisions between the Ar^+ and the target, electrons are also ejected from the target. For conductive materials the loss of negative charges is replenished by passing a DC current through the target. This does not work with insulating materials. Sputtering insulators requires RF sputtering where the voltage applied to the target oscillates between negative, to attract Ar^+ ions, and positive, to attract electrons in order to replenish the negative voltage to the target. RF sputtering works with both insulators and metals while DC sputtering only works with metals.

The sputter deposition rate depends greatly on the type of gas used, the pressure of the gas, and power dissipated in the target. For the most efficient deposition, the gas used should have the same atomic weight as the atoms of the target materials. Ar matches relatively well with the light transition metals. This maximizes the energy transfer into the target atoms, preventing the Ar atoms from reflecting off the target and impacting the substrate.

As mentioned above, the pressure of the gas in the chamber during deposition affects the deposition rate. The mean free path of the sputtered atoms is smaller at higher pressures. Collisions between the target and gas atoms change the direction and reduce the kinetic energy of the target atoms. The direction change causes atoms to miss the substrate, resulting in a small reduction of the deposition rate. Once these low energy atoms contact the surface of the substrate they do not have energy to diffuse along the surface to find the

lowest energy position leading to a rougher deposited film surface. To obtain smoother films the Ar pressure in the chamber was kept as low as possible. Deposition of Ta and Cu was at 1.7 mTorr while the magnetic layers were deposited at 2.2 mTorr.

The base pressure of the system was below 10^{-7} Torr, generally hovering around 7×10^{-8} Torr. Lower base pressure indicates that less N_2, O_2, water vapour, and organic gasses are present in the chamber. Contaminants in the deposition chamber reduce the quality of the films.

I grew two types of films for this project. The first group consisted of single layers of each element, grown specifically for calibrating the deposition rates of the sputtering guns. These calibration samples were grown on glass substrates. The second set of films I deposited are shown in Figure 2.2, were used for measuring the exchange stiffness in thin film Co and Co alloys. These were grown on Si (001). The magnetic structures consisted of a two magnetic cobalt-based, CoX, layers anti-ferromagnetically coupled across a thin Ru spacer layer, CoX/Ru/CoX. X is the alloying element, one of Cr, Fe, Ni, Pd, Pt or Ru. The magnetic layers were sandwiched between a 50 Å thick seed and capping layers both of Ru.

The Ru seed layer was deposited on top of 30 Å of either CrTa or Ta followed by 100 Å of Cu. The orientation of the Cu, Ru, and Co layers were unaffected by the choice of CrTa or Ta. Cu has a face-centred-cubic (fcc) crystal structure and grows along the [111] direction on top of Ta. Figure 2.3 shows that the atoms on the (111) planes of the fcc structure are arranged in a hexagonal pattern like those on the (0002) planes of the hcp structure. The only difference between these two structures is the way in which the sheets of atoms are stacked on top of one another (A, B, A, B ... for hcp; and A, B, C, A, B, C ... for FCC; see Figure 2.3) [29, 30]. For this reason, Ru (0002) planes grow on top of Cu (111). The polycrystalline nature of the films and the uniaxially textured with the grain aligned perpendicular to the surface. This was confirmed by measuring the Bragg peaks using X-ray diffraction. The Ru seed layer was grown in order to promote the hexagonal crystalline growth for the CoX layers and the Ru capping layer prevented oxidation of the films.

I investigated the exchange stiffness of CoX using CoX(100 Å)/Ru/CoX(100 Å) structures. I also studied the exchange stiffness of Co as a function of thickness to determine whether the differences between my results and literature values for A_{ex} and M_s are due to

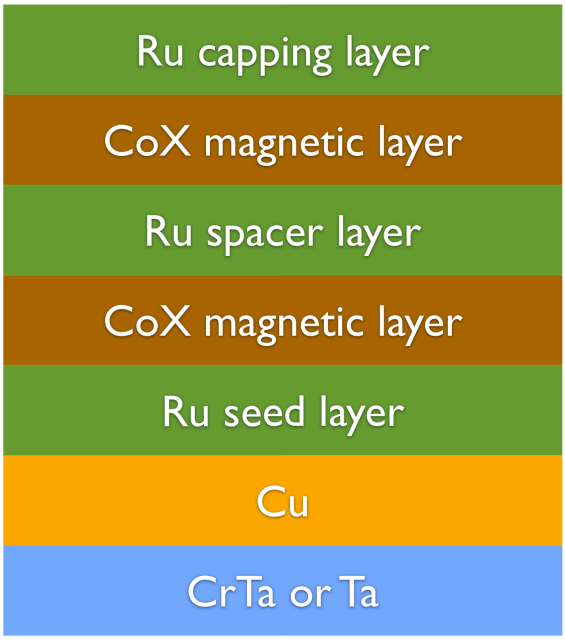

Figure 2.2: This is a cross section of the multilayer structures prepared for the measurements of A_{ex} of cobalt alloys. The structures consisted of: seed layers, made from CrTa or Ta followed by Cu and Ru; magnetic layers, comprising of two ferromagnetic CoX layers anti-ferromagnetically coupled by a Ru spacer layer; and a Ru capping layer.

surface effects of the thin films. For these experiments the Co thickness varied from 24 Å to 200 Å. The thickness of the Ru spacer layer was between 2.5 Å and 3.5 Å to optimize the RKKY coupling.

In CoX layers with more than 10% of the alloying element X, an additional 12 Å Co layer was added around the Ru spacer layer to achieve sufficiently large RKKY coupling between the CoX layers. The coupling strength varies with the Ru layer thickness and M_s. In most CoX alloys, M_s is reduced due to alloying, reducing the coupling. The saturation field is directly related to the RKKY coupling, and it is this region of the $M(H)$ curve that is used to calculate A_{ex}.

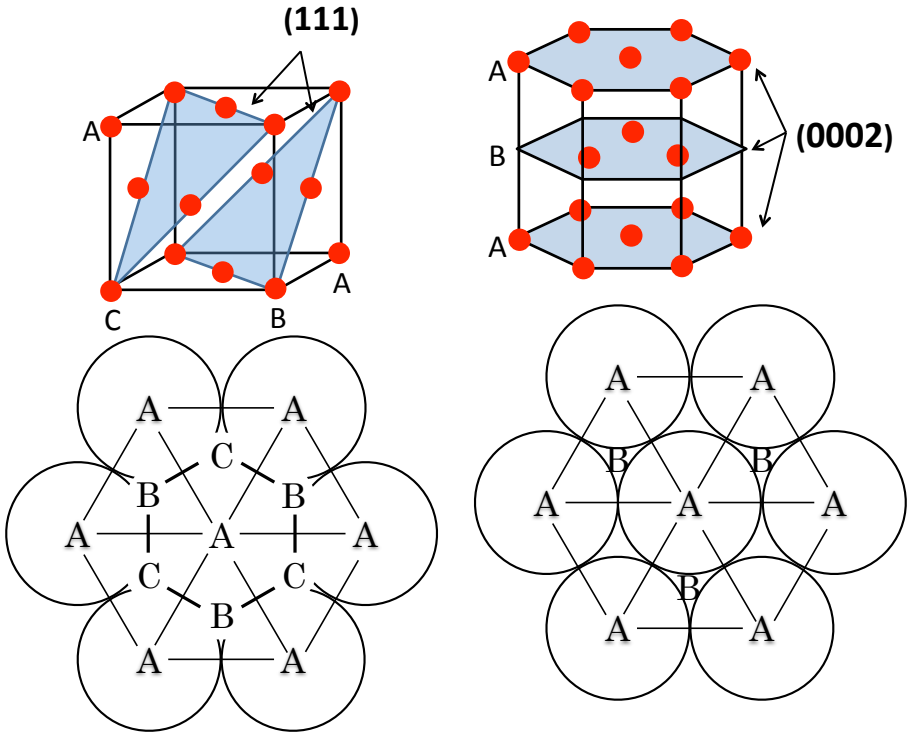

Figure 2.3: A, B, and C are atomic planes. The stacking structure of an fcc lattice is shown on the left while that of an hcp lattice is shown on the right.

2.2 Structural Characterization

The growth rates were determined from X-ray diffraction measurements of the thickness of single element films. The thickness of these layers can be calculated from Kiessig interference fringes produced by the interference of glancing incidence X-rays in a $\theta - 2\theta$ scan. A $\theta - 2\theta$ scan was also used to determine the peaks of constructive interference from atomic planes parallel to the surface of the sample. The degree of texture within the film was determined using rocking curve measurements.

In a symmetric $\theta - 2\theta$ scan, when the sample stage, and therefore the sample, is rotated so that the angle between the incident x-rays and the sample is θ, the detector is positioned to measure the intensity of the x-rays reflected from the surface. Therefore, the angle between the detector and the sample is θ and the angle between the incident beam and

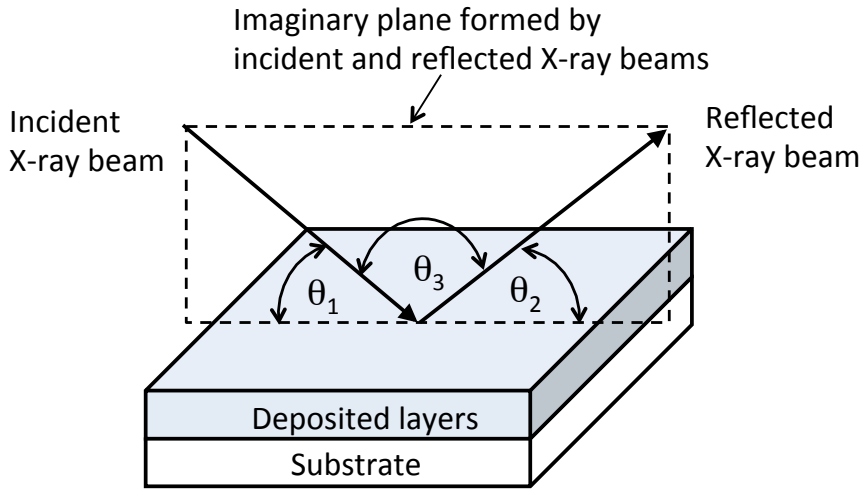

Figure 2.4: This figure shows the X-ray diffraction set up. θ_1 is the angle between the incident beam and the surface, θ_2 is the angle between the reflected beam and the surface, and θ_3 is the angle between the incident and reflected beams. For all measurements, the plane formed by the incident and reflected beams was perpendicular to the surface.

the detector is 2θ. In other words, from Figure 2.4, $\theta_1 = \theta_2 = \theta$, so that constructive interference is observed solely from reflections off atomic planes and interfaces parallel to the surface of the film allowing for measurements of the distance between atomic planes and the film thickness.

The deposited films were textured along the direction perpendicular to the surface, meaning that they had a crystal grain alignment in this direction. As mentioned previously, Cu grew along the [111] direction while Co and Ru grew along the [0002] direction. $\theta - 2\theta$ scans showed constructive interference (Bragg reflection) for: Cu (111) planes at $2\theta = 43.4^\circ$, Co (0002) planes at $2\theta = 44.39^\circ$, and Ru (0002) planes at $2\theta = 42.08^\circ$ ($\theta_1 = \theta_2 = \theta \Rightarrow \theta_1 + \theta_2 = 2\theta$). Figure 2.6 shows a polycrystalline structure where the grains grow along different crystallographic orientations. Rocking curve measurements are used to determine the preferential growth direction in the films.

After finding the Bragg reflections, 2θ, using a $\theta - 2\theta$ scan, in rocking curve measurements θ_3 is fixed at $180^\circ - 2\theta$ and θ_1 is varied. For example, the Bragg reflection for Co (0002) planes is at $2\theta = 44.39^\circ$. In rocking curve measurements θ_3 is set to $180^\circ - 2 \times 44.39^\circ$ and θ_1 was varied between $\frac{44.39^\circ}{2} \pm 15^\circ$. The full-width-half-maximum

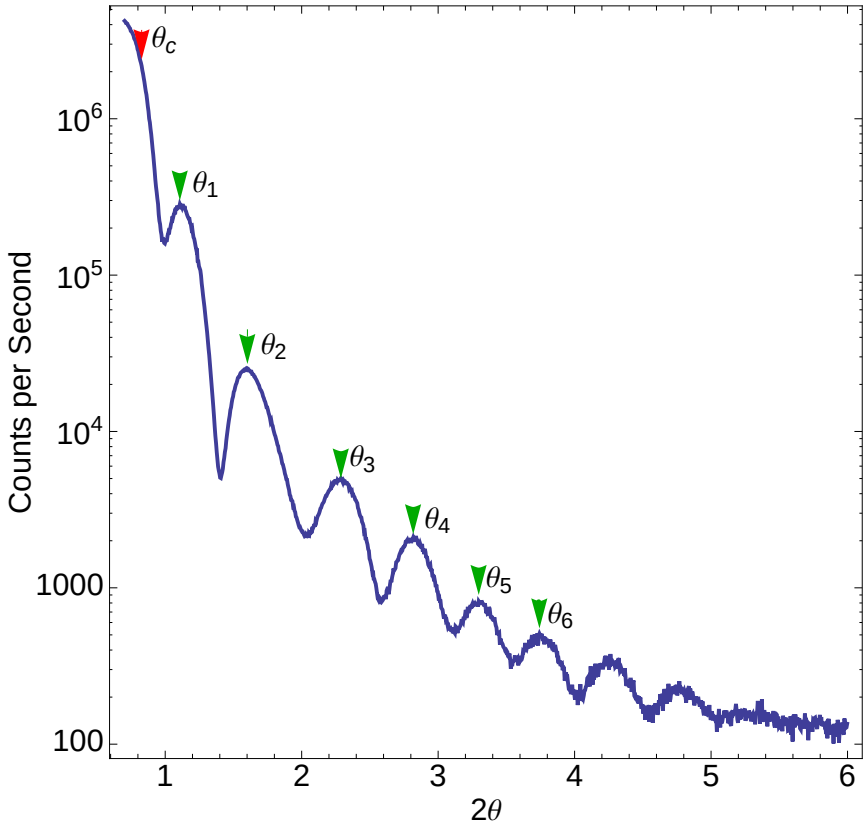

Figure 2.5: X-ray reflectivity curve from a Co film. The peaks, $\theta_1, \theta_2, \ldots$, in the reflectivity are due to constructive interference between X-rays reflected from the surface and those reflected from the interface with the substrate. θ_c is the critical angle.

(FWHM) determined by a rocking curve scan is a measure of the orientation distribution of Co (0002) planes in the film with respect to the film surface. In my films, the FWHM from Cu (111), Co (0002), and Ru (0002) was less than 4°.

Layer thickness was measured from the diffraction pattern, known as Kiessig fringes, shown in Figure 2.5, created by glancing incidence X-rays. The thickness of the deposited layers was calculated from the peak or valley positions in Figure 2.5.

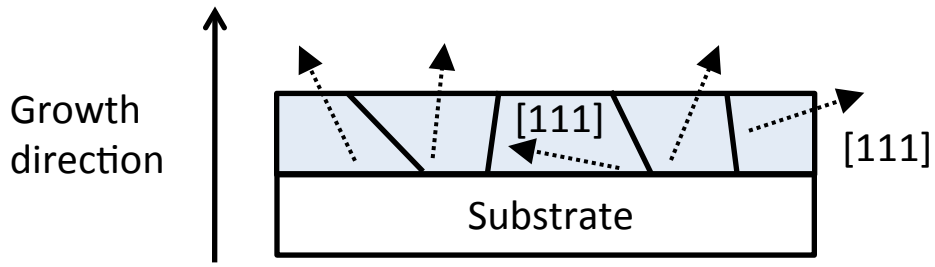

Figure 2.6: A film with polycrystalline structure where the arrows indicate the [111] direction in in each grain. In textured films the majority of the grains grow along the same crystallographic direction. X-ray diffraction measurements using a symmetric $\theta - 2\theta$ scan are only sensitive to atomic planes and interfaces parallel to the surface. The angular spread in the grain orientation is measured from the rocking curve.

2.2.1 Layer thickness from Kiessig fringes

Kiessig fringes originate from interference between x-rays reflected from the top and bottom surfaces of a film. I used Kiessig fringes from single element films to determine the thickness of these films. In order for constructive interference to occur, the optical path length difference between the two x-rays must be an integer multiple of the wavelength. The X-ray measurements were done in a Panalytical X'Pert PRO MRD that used Cu K_α X-rays with a wavelength of 1.5418 Å. The difference between Bragg and Kiessig calculations of the optical path length difference is that Kiessig's equations take into account the change in the index of refraction when calculating the optical path lengths. Figure 2.7 shows a ray diagram of the optical paths in a $\theta - 2\theta$ scan that produce Kiessig fringes.

The following derivation is used to calculate the the thickness of the layer from the interference pattern. The difference in the optical paths ΔL is given by:

$$\Delta L = n_1 (AB + BC) - AE, \tag{2.1}$$

where AB, BC, and AE are line segments between the points labeled in Figure 2.7. The condition required for constructive interference is $\Delta L = m\lambda$, where m is the order of the interference fringe and λ is the wavelength. The refracted angle, θ_1, from Figure 2.7 can be determined from: the incident angle, θ; the index of refraction of air, $n = 1$; and the index of refraction of the material, n_1:

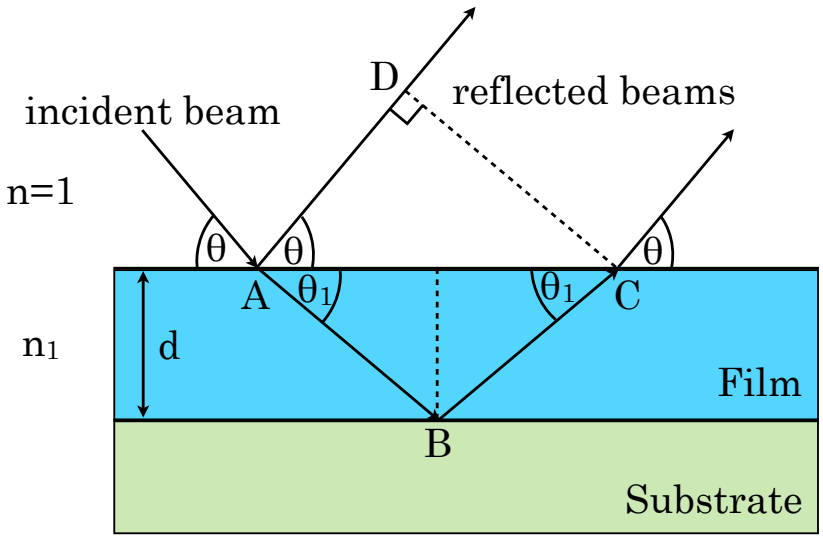

Figure 2.7: Two different x-ray paths through a single layer are shown: one that reflects from the top and one from the bottom surface. θ is the angle of the X-ray in air with respect to the sample surface and θ_1 is the refracted angle in the film. The index of refraction of the film is n_1. The thickness of the film is given by d. For constructive interference the optical path difference between these two paths must be an integer multiple of the wavelength.

$$\cos(\theta_1) = \frac{n\cos(\theta)}{n_1} = \frac{\cos(\theta)}{n_1}. \tag{2.2}$$

In the materials we measured, the index of refraction of a Cu k_α X-ray is less than 1. This does not mean that the speed of the x-ray, given by the group velocity, is faster than the speed of light, but that the phase velocity of the x-ray is greater than c [31]. Consequently, n_1 can be rewritten in terms of the critical angle, θ_c:

$$n_1 = \frac{n\cos(\theta_c)}{\cos(0)} = \cos(\theta_c). \tag{2.3}$$

The path lengths AB and BC from Equation 2.1 are identical and equal to:

$$AB = BC = \frac{d}{\sin(\theta_1)}, \tag{2.4}$$

where d is the thickness of the film. The path length AE is related to AC which can be calculated from AB:

$$AE = AC\cos(\theta) = 2AB\cos(\theta_1)\cos(\theta). \tag{2.5}$$

Equation 2.1 can now be rewritten in terms of Equation 2.4 and Equation 2.5 with the interference peaks labeled by an incident angle, θ_m:

$$m\lambda = \frac{2n_2 d}{\sin(\theta_1)} - \frac{2d}{\sin(\theta_1)}\cos(\theta_1)\cos(\theta_m). \tag{2.6}$$

Using both Equation 2.6 and Equation 2.2 as well as the identity $\sin^2(x)+\cos^2(x)=1$, this can be rewritten as:

$$m\lambda = \frac{2n_2 d}{\sin(\theta_1)}\left(1-\cos(\theta_1)^2\right) = 2dn_2\sqrt{1-\cos^2(\theta_1)}, \tag{2.7}$$

the index of refraction is replaced by the critical angle from Equation 2.3 and θ_1 is replaced using Equation 2.2 to give:

$$m\lambda = 2d\cos(\theta_c)\sqrt{1-\frac{\cos^2(\theta_m)}{\cos^2(\theta_c)}} = 2d\sqrt{\cos^2(\theta_c)-\cos^2(\theta_m)}. \tag{2.8}$$

This last equation easily reduces to the equation for calculating the thickness of a layer based on the peak position of the Kiessig fringes:

$$m\lambda = 2d\sqrt{\sin^2(\theta_m)-\sin^2(\theta_c)}. \tag{2.9}$$

I estimated the critical angle from Figure 2.5 by identifying the position at which the intensity is half the maximum value. The thicknessed of the films were calculated from the slope of $\frac{m\lambda}{2}$ versus $\sqrt{\sin^2(\theta_m)-\sin^2(\theta_c)}$.

2.3 Magnetometry

The exchange stiffness was determined by fitting a micromagnetic model to experimental measurements of the magnetization of a trilayer ferromagnet/normal metal/ferromagnet structure. The magnetization data, $M(H)$ curves, were obtained using either a superconducting quantum interference device, SQUID, or a vibrating sample magnetometer, VSM. The next two sections provide some background on the principles behind these measurement techniques.

2.3.1 SQUID

A SQUID is a very sensitive magnetic flux-to-voltage tranducer [11, 32, 33]. It is used to measure the change in the magnetic flux using two Joesphson junctions that are connected in parallel, as shown in Figure 2.8. A Josephson junction is a thin insulating barrier separating two superconductors. In order to measure a flux the SQUID is biased above the critical current of the Josephson junctions so that they are resistive. When the magnetic flux through the SQUID is non-zero a screening current circulates in the SQUID to oppose this magnetic field. Due to the single valued nature of the electron wavefunction around the loop, the screening current, and consequently the allowed flux through the SQUID, are quantized.

The pick up loop shown in Figure 2.8 consists of three coils, SC1, SC2, and SC3 all of which are superconducting. As the magnetic sample is moved through the two oppositely wound coils, SC1 and SC2, a current is generated in the pick up loop to account for the change in the flux through the coils. This same current flows in SC3 and generates a magnetic field that is applied to the SQUID. This changes the magnetic flux through the SQUID and consequently the voltage across the SQUID. The potential difference across the SQUID is fed into a feedback circuit known as a flux-locked-loop, which applies an additional field via the flux-locked-loop coil to the SQUID to return it to its initial state. The magnetization of the sample is determined by measuring the current in the flux-locked-loop.

2.3.2 VSM

A VSM is used to measure the magnetization of a sample [35]. A magnetic sample is attached to a voice coil by a rigid rod and then placed inside a uniform magnetic field. A cut away diagram showing the experimental set up of a VSM is shown in Figure 2.9. The voice coil drives sinusoidal oscillations of the sample within the uniform magnetic field. These oscillations produce a time dependent magnetic flux through two oppositely wound pick-up coils that in turn induces a voltage in the coils due to Faraday's law. This induced voltage is measured using a lock-in amplifier tuned to the driving frequency of the voice coil. The magnitude of this voltage is related to the frequency and amplitude of the oscillations as well as the total magnetization of the sample. In these measurements,

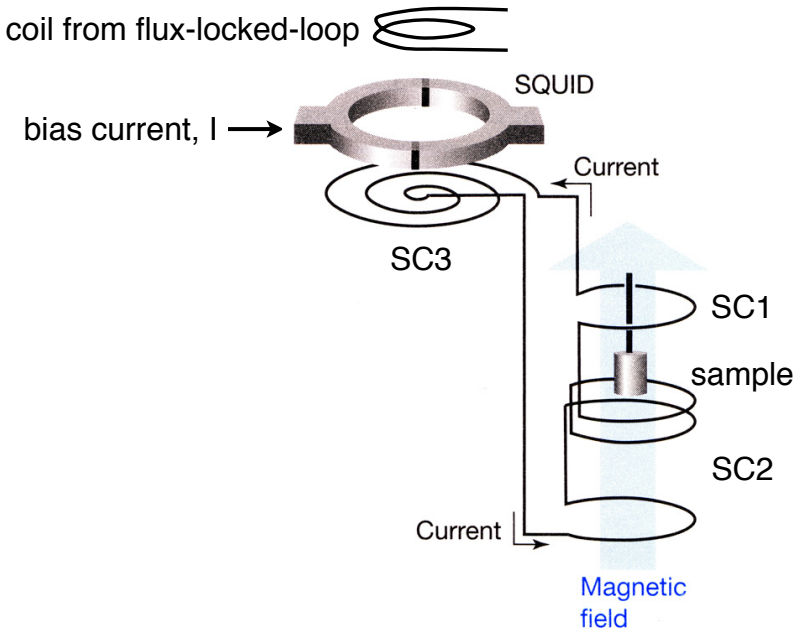

Figure 2.8: A DC SQUID is made from a the parallel configuration of two Josephson Junctions in a superconducting loop. Magnetic flux through the loop induces a circulating current in the loop. The boundary conditions on the wavefunction quantizes the flux which can pass through the loop. By biasing the SQUID above the critical current of the Josephson Junction, the SQUID becomes resistive and Ohm's law is used to determine the current and hence the flux in the loop. This is a modified version of a figure from Yasin [34].

the frequency is held constant, and the oscillation amplitude is measured using a reference magnet in a separate set of pick-up coils. The VSM was calibrated using a reference sample measured with a SQUID magnetometer.

2.4 X-ray Magnetic Circular Dichroism (XMCD)

XMCD is the measurement of the difference in the absorption of left- and right-handed circularly polarized X-rays by a magnetic sample [36]. In XMCD measurements, core electrons are excited by left- and right-handed circularly polarized X-rays into empty states above the Fermi energy to probe the magnetic properties of the empty valence levels. In

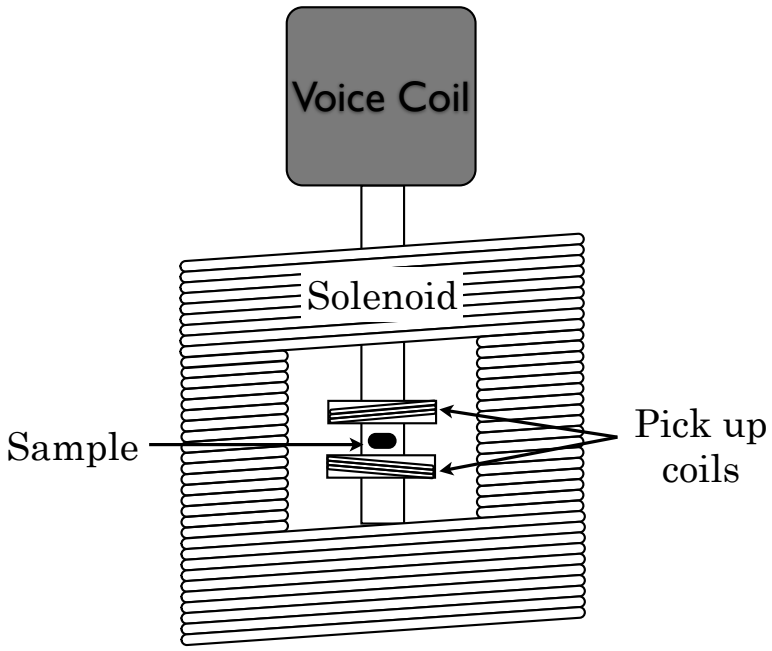

Figure 2.9: A VSM can be used to measure the magnetization of magnetic samples. A voice coil drives sinusoidal oscillations of a magnetic sample through two oppositely wound pick up coils. The time dependent flux through the coils creates a potential difference across the coils according to Faraday's Law.

CoX alloys, the magnetic properties are largely determined by the 3d valence electrons (note that for Ru and Pd magnetic properties are determined by 4d and for Pt by 5d electrons). Since X-ray absorption spectra are governed by dipole selection rules the d-shell properties are best probed by exciting electrons from the p level into the d. The p to d transition energy is different for different elements. Therefore the occupation of the d valence electrons for each element in the CoX alloy can be measured independently, and therefore the contribution of each element to the total magnetization.

During electron excitation due to photon absorption both the energy and the angular momentum of the photon are transferred to the electron. Due to spin orbit coupling, the angular momentum of the photon can be transferred to the spin of the electron. This effectively results in spin polarization of the excited electrons. For example, for right hand circularly polarized light at the L2 edge 75% of the excited electrons are spin down, and at the L3 edge 62.5% of the excited electrons are spin up. The spin polarization is differently

oriented at the L2 and L3 edges due to the difference in the spin orbit coupling, l+s, at L3 and, l-s, at L2. Figure 2.10 shows this excitation process. The unequal number of spin up and spin down electrons in the d orbital produces an unequal absorption cross section for the two X-ray polarization directions. The magnetic moment of individual elements in an alloy was determined from the difference in the absorption of the two polarizations of photons within the range of energies that match the p to d transition of the investigated element. These measurements were performed by Olof Karis.

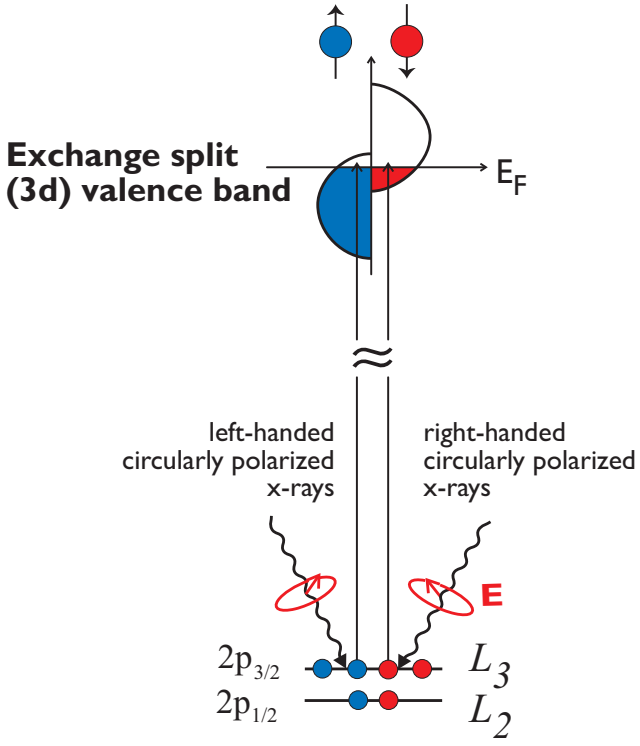

Figure 2.10: In XMCD measurements the circularly polarized light excites a spin polarized electrons from 2p level. These spin polarized electrons are used to probe occupation of 3d states. From Knut [36]; used with permission from his supervisor Olof Karis.

Chapter 3

Theoretical Background

3.1 Magnetic Energy

The magnetization distribution in an isolated ferromagnet in an external magnetic field is determined by minimizing the total magnetic energy (E_{Mag}). The energy terms that contribute to E_{Mag} are: the exchange energy (E_{ex}), the Zeeman energy (E_Z), the anisotropy energy (E_{An}), and the demagnetization energy (E_D) [37]. In systems where two ferromagnets are separated by a thin normal metal spacer layer, like the magnetic structures grown for this thesis, the two layers may also be coupled by the Ruderman-Kittel-Kasuya-Yosida (RKKY) interaction [10]. This interaction will affect the magnetization distribution in CoX/Ru/CoX films, and therefore is included in the total magnetic energy:

$$E_{Mag} = E_{ex} + E_Z + E_{An} + E_D + E_{RKKY}. \tag{3.1}$$

3.1.1 Exchange Interaction

The exchange interaction was first proposed by Heisenberg in 1928 to explain the large magnetic fields found in ferromagnetic materials [38]. The Heisenberg Hamiltonian is:

$$H_{Heisenberg} = -J \sum_{<ij>} \vec{S}_i \cdot \vec{S}_j, \tag{3.2}$$

where the sum is over all neighbouring spin pairs <ij> with an exchange coupling J. Before 1928, the physics behind ferromagnetism was not well understood [10]. The classical picture involving the dipolar interactions aligning neighbouring spins was not able to explain the coupling given the weakness of this interaction [38]. The exchange interaction is a purely quantum mechanical effect that follows directly from the Pauli exclusion principle thereby linking the spin-spin interaction with the Coulombic interaction between two particles [38].

The wavefunction of a two electron system may be approximated as the product of the individual wavefunctions of the electrons. These wavefunctions consist of two parts, a spatial part, φ, that depends on the electron's position, $\vec{r}$, and a spin part, χ, that depends on the electron's spin, σ. The wavefunctions pertaining to the individual electrons can be identified with subscripts so that the total wavefunction is:

$$\Psi(\vec{r}_1,\vec{r}_2,\sigma_1,\sigma_2) = \varphi(\vec{r}_1,\vec{r}_2)\chi(\sigma_1,\sigma_2). \tag{3.3}$$

The Pauli exclusion principle states that upon the exchange of two electrons the wavefunction of the system must be antisymmetric [39]. Thus, Pauli exclusion requires that one of φ or χ from Equation 3.3 must be symmetric under exchange while the other must be antisymmetric:

$$\left.\begin{aligned}\varphi(\vec{r}_1,\vec{r}_2) &= -\varphi(\vec{r}_2,\vec{r}_1)\\ \chi(\sigma_1,\sigma_2) &= \chi(\sigma_2,\sigma_1)\end{aligned}\right\} \tag{3.4a}$$

or

$$\left.\begin{aligned}\varphi(\vec{r}_1,\vec{r}_2) &= \varphi(\vec{r}_2,\vec{r}_1)\\ \chi(\sigma_1,\sigma_2) &= -\chi(\sigma_2,\sigma_1).\end{aligned}\right\} \tag{3.4b}$$

These two possible electron configurations produce two different electrostatic energies. The antisymmetric spin configuration requires that the electrons have different quantum numbers. As they are in different spin states, Pauli exclusion does not prevent them from overlapping. The symmetric spin wavefunction implies that the electrons are in the same state and therefore the wavefunctions cannot overlap. Larger spacing between the electrons in Equation 3.4a compared to Equation 3.4b reduces the Coulombic potential.

The possible symmetric, φ_s, and antisymmetric, φ_a, spatial wavefunctions for a two electron system are

$$\varphi_s(\vec{r_1},\vec{r_2}) = \frac{1}{\sqrt{2}}[\varphi_1(\vec{r_1})\varphi_2(\vec{r_2}) + \varphi_1(\vec{r_2})\varphi_2(\vec{r_1})] \tag{3.5a}$$

$$\varphi_a(\vec{r_1},\vec{r_2}) = \frac{1}{\sqrt{2}}[\varphi_1(\vec{r_1})\varphi_2(\vec{r_2}) - \varphi_1(\vec{r_2})\varphi_2(\vec{r_1})] \tag{3.5b}$$

The Hamiltonian for the spatial wavefunctions is:

$$H = \sum_i^2 \left[\frac{-\hbar^2}{2m}\nabla_i^2 - \frac{Z_i e^2}{4\pi\varepsilon_0 r_i}\right] + \frac{e^2}{4\pi\varepsilon_0 r_{12}}, \tag{3.6}$$

where the sum is over both electrons, r_i is the position of the i^{th} electron, r_{12} is the distance between the electrons. Therefore, the energy difference between the states given by Equation 3.5a and Equation 3.5b is:

$$E_{s-a} = \int \varphi_s^* H \varphi_s - \int \varphi_a^* H \varphi_a = 2J_{12}, \tag{3.7}$$

where J_{12} is the energy of the electron-electron interaction [38]. The energy difference is related only to the relative orientation of the spins. One arrives at the same energy difference between symmetric and antisymmetric states using Equation 3.2:

$$\begin{aligned} E_{\uparrow\uparrow} &= -JS_1S_2 \\ E_{\uparrow\downarrow} &= JS_1S_2 \\ E_{\uparrow\uparrow} - E_{\uparrow\downarrow} &= -2JS_1S_2, \end{aligned} \tag{3.8}$$

provided that J_{12} accounts for the product of the spins.

Exchange Stiffness Constant

The coupling term J from Equation 3.2 is a measure of the strength of the exchange interaction between two spins. As it does not account for the number of nearest neighbour pairings, a better term for cross material comparison is the exchange stiffness, A_{ex}. The exchange stiffness is a material specific magnetic energy parameter that includes the exchange coupling J, the number of nearest neighbours, and the distance between the neigh-

bours. What follows is a derivation of the exchange stiffness constant based on that done by Chikazumi [38].

In Figure 3.1, $\hat{\alpha}$ is a unit vector parallel to the direction of the spin of an atom. The derivation that follows, calculates the expression for the exchange stiffness in terms of the exchange coupling, the spin, and lattice parameters. This expression will be substituted into the exchange energy to obtain a hamiltonian for the micromagnetic calculations.

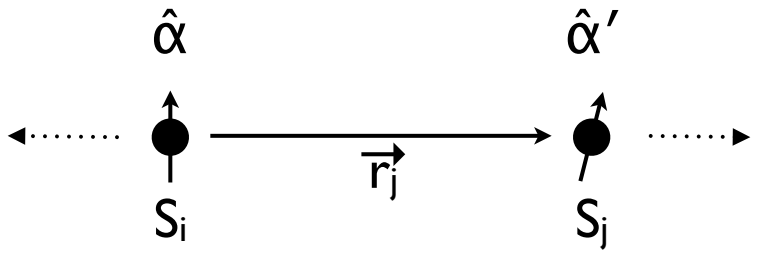

Figure 3.1: The Heisenberg Hamiltonian calculates the magnetic energy of a ferromagnet from the exchange interaction between nearest neighbour atomic pairs. This figure shows one such atomic pair separated by a vector $\vec{r}_j$ [38]. The atoms have spins S_i and S_j. The normalized vectors $\hat{\alpha}$ and $\hat{\alpha}$ are parallel to the spin directions of the respective atoms.

The energy, W_{ij}, of an interacting pair of spins like that shown in Figure 3.1 is calculated from the Heisenberg Hamiltonian, as:

$$\begin{aligned} W_{ij} &= -2J\vec{S}_i \cdot \vec{S}_j \\ &= -2JS^2\hat{\alpha(i)} \cdot \hat{\alpha(j)} \\ &= -2JS^2\cos(\phi) \\ &\approx -2JS^2 + JS^2\phi^2, \end{aligned} \tag{3.9}$$

where $\vec{S}_i$ and $\vec{S}_j$ are the spins of the two atoms, S is the magnitude of the spin, and ϕ is the angle between the two spin directions. Assuming a uniform variation in the spin directions, $\hat{\alpha(j)}$ at $\vec{r}_j = x_j\hat{i} + y_j\hat{j} + z_j\hat{k}$, $\hat{\alpha(j)}$, can be calculated from a Taylor series expansion of $\hat{\alpha(i)}$:

$$\hat{\alpha(j)} = \hat{\alpha(i)} + \left(\frac{\partial\hat{\alpha}}{\partial x}x_j + \frac{\partial\hat{\alpha}}{\partial y}y_j + \cdots\right) + \frac{1}{2}\left(\frac{\partial^2\hat{\alpha}}{\partial x^2}x_j^2 + \frac{\partial^2\hat{\alpha}}{\partial y^2}y_j^2 + \cdots\right). \tag{3.10}$$

The scalar product of two neighbouring spin directions then becomes:

$$\hat{\alpha(i)} \cdot \hat{\alpha(j)} = \hat{\alpha(i)} \cdot \hat{\alpha(i)} + \hat{\alpha(i)} \cdot \left(\frac{\partial \hat{\alpha}}{\partial x} x_j + \frac{\partial \hat{\alpha}}{\partial y} y_j + \cdots \right) + \frac{\hat{\alpha(i)}}{2} \cdot \left(\frac{\partial^2 \hat{\alpha}}{\partial x^2} x_j^2 + \frac{\partial^2 \hat{\alpha}}{\partial y^2} y_j^2 + \cdots \right). \tag{3.11}$$

The first term in Equation 3.11 does not depend on the spin of the atom at j and therefore represents an energy shift that can be neglected. The second term does not contribute to the total energy since the energy contribution from the two nearest neighbours in the chain are equal in magnitude but opposite in sign. Thus, the total energy of an atom in a lattice with n nearest neighbours is given by:

$$E = -JS^2 \sum_{j=1}^{n} \hat{\alpha} \cdot \left(\frac{\partial^2 \hat{\alpha}}{\partial x^2} x_j^2 + \frac{\partial^2 \hat{\alpha}}{\partial y^2} y_j^2 \cdots \right). \tag{3.12}$$

For simple cubic (sc), body-centred cubic (bcc), and face-centred cubic (fcc) lattices the summation in Equation 3.12 simplifies because:

$$\sum_{j=1}^{n} x_j^2 = \sum_{j=1}^{n} y_j^2 = \sum_{j=1}^{n} z_j^2 = 2a^2, \tag{3.13}$$

where a is the lattice constant of either a sc, bcc, or fcc structure. For example, in an fcc lattice every atom has 12 equally spaced nearest neighbours. They occupy: 4 positions at (±a/2,±a/2,0), 4 positions at (±a/2,0,±a/2), and 4 positions at (0,±a/2,±a/2). Then considering a summation over the x component, $\sum_{j=1}^{n} x_j^2 = 8 \times a^2/4 = 2a^2$. The same is true for the y and z components. The investigated CoX films were all hcp structures. This structure has also 12 equally spaced nearest neighbours. The [0002] direction of a hcp structure is the same as the [111] direction of an fcc lattice, so, for simplifity, I assumed that the expression of A_{ex} for a hcp lattice is the same as that of a fcc structure. This is a valid because the micromagnetic model I developed is per unit area, in other words, based on a 1D spin chain. In this case, the only relevant detail about the crystal structure is the distance between the atoms and this parameter is included in the model. The energy density, ε, for a single atom resulting from the exchange interaction in a cubic lattice using the results of Equation 3.12 and Equation 3.13 becomes:

$$\varepsilon_{ex} = \frac{1}{2V} E = \frac{-2a^2 nJS^2}{2V} \hat{\alpha} \cdot \left(\frac{\partial^2 \hat{\alpha}}{\partial x^2} + \frac{\partial^2 \hat{\alpha}}{\partial y^2} \cdots \right) \tag{3.14}$$

where V is the volume of a unit cell. In a cubic lattice $V = a^3$. Equation 3.14 includes an additional factor of $\frac{1}{2}$ to adjust for the double counting. Starting from $(\hat{\alpha} \cdot \hat{\alpha}) = 1$ and differentiating this equation twice with respect to x it follows that $\hat{\alpha} \cdot \frac{\partial^2 \hat{\alpha}}{\partial x^2} = -\left(\frac{\partial \hat{\alpha}}{\partial x}\right)^2$. Equation 3.14 can be written as:

$$E_{ex} = \frac{nJS^2}{a}\left[\left(\frac{\partial \hat{\alpha}}{\partial y}\right)^2 + \left(\frac{\partial \hat{\alpha}}{\partial y}\right)^2 + \left(\frac{\partial \hat{\alpha}}{\partial z}\right)^2\right], \tag{3.15a}$$

where

$$A_{ex} = \frac{nJS^2}{a}. \tag{3.15b}$$

Equation 3.15b shows that A_{ex} is proportional to the product of the number of nearest neighbours, n, the exchange integral, J, and square of spin, S^2, and is inversely proportional to the lattice constant, a, and therefore the distance between the spins.

In developing the micromagnetic model, I assumed that the exchange interaction acted solely between neighbouring atomic planes in the CoX layers. It was also assumed that the magnetization in each atomic plane rotates uniformly, i.e. each atomic plane was treated as a macrospin. In this case, Equation 3.9 can be used to model the exchange interaction between the layers. The only difference is that in the micromagnetic model has to include the number of nearest neighbours that interact per unit area. Given that an atom has n nearest neighbours in an area a^2 the energy per unit area of a magnetic layer containing N atomic planes is:

$$E_{ex} = \sum_{i=1}^{N} \frac{nW_{i,i+1}}{a^2}. \tag{3.16}$$

Using Equation 3.9 for the definition of W_{ij}, Equation 3.16 becomes:

$$E_{ex} = \frac{n}{a^2} \times -2JS^2 \sum_{i=1}^{N} \cos(\theta_i - \theta_{i+1}) = \frac{-2}{a} \times \frac{nJS^2}{a} \sum_{i=1}^{N} \cos(\theta_i - \theta_{i+1}), \tag{3.17}$$

where θ_i and θ_{i+1} are the magnetization angles of a macrospins in atomic planes i and $i+1$. From the defintion of the exchange stiffness in Equation 3.15b, Equation 3.17 reduces to:

$$E_{ex} = \frac{-2A_{ex}}{d} \sum_{i=1}^{N} \cos(\theta_i - \theta_{i+1}), \tag{3.18}$$

which is the equation for the exchange energy of a magnetic layer with N atomic planes. In this equation, the lattice constant a has been replaced with d to represent the distance between the atomic planes.

3.1.2 RKKY Interaction

Magnetic layers separated by thin normal metal spacer layer experience an exchange coupling whose strength, J_{RKKY}, decays and sign oscillates with increasing thickness of the spacer layer as shown by several experiments including Girt and Richter [40]. Figure 3.2 shows both my and Girt's and Richter's [40] measurements of J_{RKKY} as a function of Ru layer thickness. These values were calculated using the same micromagnetic model used to calculate A_{ex}. I was interested in large antiferromagnetic coupling between CoX layers. For this reason I explored only a very narrow range of Ru thicknesses from about 3 to 5 Å where the antiferromagnetic coupling is the largest.

In metals the Fermi surface marks a sharp cut-off between occupied and unoccupied states at 0 K. This results in spatial oscillations of the electrons in response to a localized perturbation [41–43]. In the case of a magnetic perturbation in a normal metal, the oscillations will be in the electron spin density of the material [41]. Ruderman and Kittel [44] were the first to propose that oscillations in the spin density coupled magnetic impurities in normal metals. This theory was expanded to explain magnetic coupling between ferromagnetic layers separated by normal metal layers [41–43].

In ferromagnet/normal metal/ferromagnet (FM/NM/FM) structures, the magnetic perturbation in the normal metal is the result of coupling between the ferromagnet and the normal metal at the interface through the s-d Hamiltonian [42, 45]:

$$H_{sd} = -J_{sd}\vec{m}\cdot\vec{n}\delta(\vec{r}), \tag{3.19}$$

where J_{sd} is the effective exchange coupling, $\vec{m}$ is the magnetic moment in the ferromagnetic layer, $\vec{n}$ is the magnetic moment in the normal metal layer, and $\delta(\vec{r})$ indicates the position of the interface. In my structures, FM/NM interfaces are between the CoX magnetic layers and the Ru spacer layer. From Equation 3.19 positive values of J_{sd} favor ferromagnetic alignment between $\hat{m}$ and $\hat{n}$ at the FM/NM interfaces. Away from the FM/NM interfaces, the induced moments in the NM oscillate across the spacer layer. De-

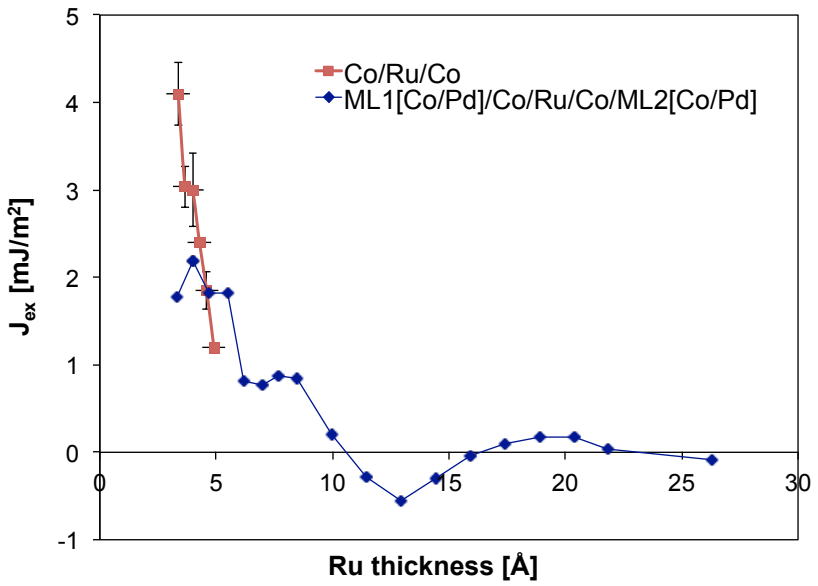

Figure 3.2: The data presented in this plot, measured by Girt and Richter [40] shows the decaying and oscillatory nature of RKKY coupling between ferromagnetic layers separated by a normal metal spacer layer. I also calculated J_{RKKY} as a function of Ru thickness in Co/Ru/Co using the same micromagnetic model used to determined A_{ex}. We varied Ru thickness in a narrow range from 3 to 5 Å to explore the region of maximum antiferromagnetic RKKY coupling.

pending on the phase of the oscillations this will impose either ferromagnetic coupling, shown in the top figure of Figure 3.3, or antiferromagnetic coupling, shown in the bottom figure of Figure 3.3.

The energy of this interaction per unit area is proportional to the coupling constant, J_{RKKY}, and the direction of the magnetic moments in the ferromagnetic layers $\hat{m_1}$ and $\hat{m_2}$[42]:

$$E_{RKKY} = J_{RKKY}\hat{m_1}\cdot\hat{m_2}. \tag{3.20}$$

Positive values of J_{RKKY} favoured antiferromagnetic coupling, so the minimum energy arises when $\hat{m_1}\cdot\hat{m_2} = -1$.

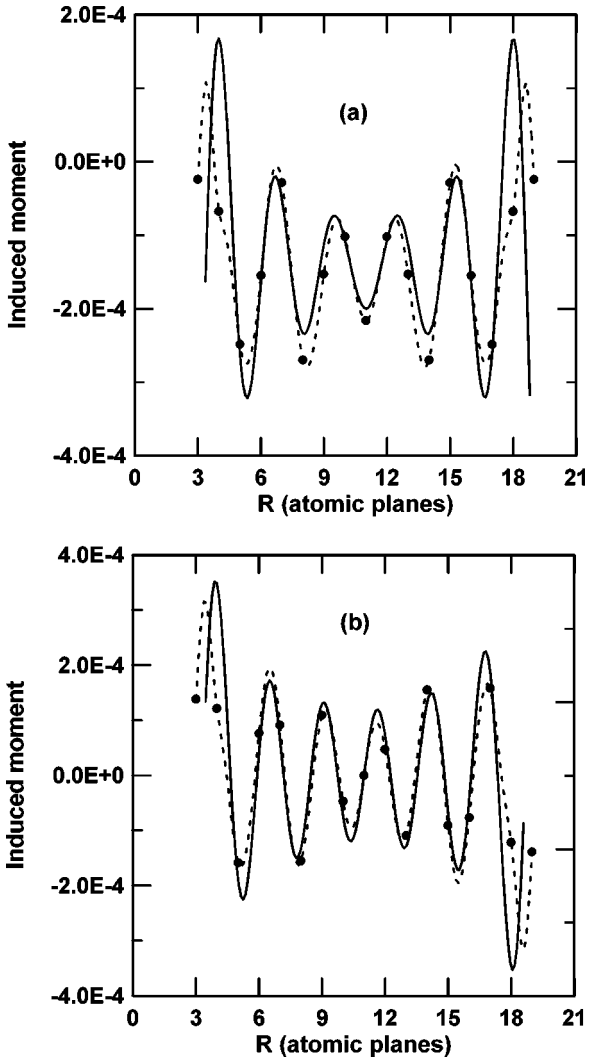

Figure 3.3: Density function theory calculations of the induced moment within the normal metal as a function of the distance from the FM/NM interfaces in an FM/NM/FM structure. The induced moments are higher density regions of a either spin up or spin down electrons. The upper figure shows the spin density oscillations in the normal metal that is ferromagnetically coupling two ferromagnets while the lower figure shows the antiferromagnetically coupled case. Note at the FM/NM interface the direction of magnetic moment in the ferromagnetic layer, $\hat{m}$, is parallel to the direction of the magnetic moment in the normal metal, $\hat{n}$. Planes 3 to 19 are the normal metal. From Mathon et al. [46]; used with permission.

3.1.3 Zeeman energy

The Zeeman energy arises from interactions between a magnetized system and an applied external field. The forces applied by the magnetic field are torsional, rotating the magnetic moments to align with the magnetic field lines [47]. In the most general case the Zeeman energy is calculated from:

$$E_Z = -\int_V \vec{M} \cdot \vec{H} dV, \tag{3.21}$$

where V is the volume of the magnetic material, $\vec{M}$ is the magnetization of the sample, and $\vec{H}$ is the applied external field[Chikazumi].

This equation simplifies dramatically under the assumptions that both the magnetization and the applied fields are homogeneous. In this case the energy becomes:

$$E_Z = -M_s H V \cos(\theta_M - \theta_H), \tag{3.22}$$

where θ_M and θ_H are the angles of the magnetization and applied field respectively. In magnetic layers that I investigated each atomic plane reverses coherently in the presence of external magnetic field. In this case the total Zeeman energy per unit area of magnetic layer consisting of N atomic planes is:

$$E_Z = -M_s H d \sum_{i=1}^{N} \cos(\theta_i - \theta_H), \tag{3.23}$$

where d is the distance between atomic planes.

3.1.4 Anisotropy and Demagnetization Energies

The magnetic anisotropy energy is the energy associated with the directional dependence of the magnetization of a ferromagnet. Anisotropy can originate in crystalline ferromagnets that have crystallographic directions along which the magnetization preferentially orients [37, 38]. These directions are known as easy axes. The symmetry of the anisotropy energy must at least match that of the crystal. In the case of hcp crystalline structure, like that of Co, the easy axis is parallel to the c-axis of the crystal. This uniaxial anisotropy energy can be expressed in terms of: the anisotropy constants: K_{u1}, K_{u2}, and K_{u3}, and the angle between the easy axis and the magnetization direction, θ [38]:

$$E_{An} = K_{u1}\sin^2(\theta) + K_{u2}\sin^4(\theta) + K_{u3}\sin^6(\theta) + \cdots . \tag{3.24}$$

The anisotropy field is the magnetic field strength that aligns the magnetization along a given axis. It is directly related to the anisotropy and M_s by $H_{An} = \frac{2K_{u1}}{M_s}$. The anisotropy field can be used instead of the anisotropy energy to determine the magnetization direction in a ferromagnet. K_{u1} for Co is 3×10^6 erg/cm^3 and the M_s is 1250 emu/cm^3, therefore the H_{An} for Co is 4.8 kOe.

In a uniformly magnetized film, the magnetic field produced by the free poles at the external edge of the sample is opposite to the direction of the magnetization in the sample. This field is called the demagnetization field, $H_D = NM_s$, where N is the demagnetizing factor. N is dependent on the sample shape. In thin films, if the magnetization is perpendicular to the surface $N = 4\pi$. Therefore, the demagnetization field for thin Co films is:

$$H_D = NM_s = 4\pi \times 1250 emu/cm^3 = 15.7 kOe. \tag{3.25}$$

In thin film Co layers, the demagnetization field is much larger than the uniaxial anisotropy field forcing the magnetic moments to lie in-plane. This result is in agreement with the conclusion of Brandenburg et al. [48] that the demagnetization field is larger than the anisotropy energy in Co films thinner than 39 nm.

3.2 Micromagnetic Model

For these experiments, I investigated the magnetic behaviour of a FM/NM/FM tri-layer structure, where the ferromagnetic (FM) layers are antiferromagnetically coupled via the RKKY interaction across a non-magnetic (NM) spacer layer. In this structure, all layers are highly textured along the [0001] direction of the hcp crystal structure, i.e., the [0001] direction is oriented perpendicular to the film surface. The uniaxial magnetocrystalline anisotropy in the FMs is aligned along the [0001] direction. I considered the case where the external magnetic field is applied parallel to the surface of the films and the shape anisotropy in the FMs is much larger than the magnetocrystalline and surface anisotropies, forcing the magnetic moments to lie in the film plane. The calculations of the anisotropies

in the last section confirm that these are reasonable assumptions. I also assumed that there was no additional in-plane anisotropy in the FM layers.

Provided the investigated film structures are uniform perpendicular to the film's growth direction, the magnetization reversal in these structures can be described by a one dimensional micromagnetic model. In this model, each FM layer consists of N magnetic atomic planes that interact only with their nearest vertical neighbours through the direct exchange interaction. I also assumed that the magnetic moments in each atomic plane rotate coherently. In this case, competition between the Zeeman, RKKY, and exchange energies creates a spin spiral in each FM layer, as shown in Figure 3.4. In the model, the atomic planes were separated by 2 Å, which is half the lattice constant c of Co.

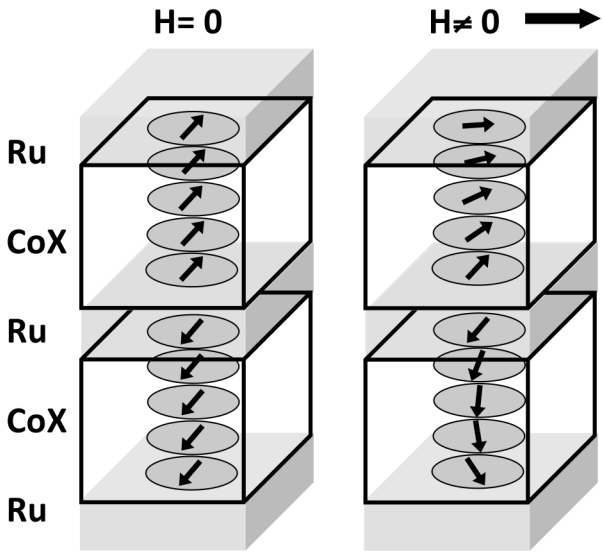

Figure 3.4: This figure qualitatively demonstrates the formation of the exchange spring of a tri-layer system when subjected to an external magnetic field as predicted by the micromagnetic model. I assumed that the spins in each atomic plane rotated coherently.

The direction of the magnetic moment in each magnetic sub-layer in the FM layers as a function of the external magnetic field is then calculated by minimizing the total magnetic energy per unit area. The total magnetic energy of the system, E_{Mag}, can be written as:

Single Layer Model

$$
\begin{aligned}
E_{Mag} &= E_{RKKY} - E_{ex} - E_Z \\
E_{RKKY} &= J_{RKKY}\cos(\theta_N - \theta_{N+1}) \\
E_{ex} &= \frac{2A_{ex}}{d}\left[\sum_{i=1}^{N-1}\cos(\theta_i - \theta_{i+1}) + \sum_{i=N+1}^{2N-1}\cos(\theta_i - \theta_{i+1})\right] \\
E_Z &= M_s H d \sum_{i=1}^{2N}\cos(\theta_i - \theta_H),
\end{aligned}
\tag{3.26}
$$

The RKKY coupling acts solely between the ferromagnetic atomic planes bordering the non-magnetic spacer layer. E_{ex}, derived in Equation 3.18, represents the energy contribution from the direct exchange interaction between nearest neighbour atomic planes within each magnetic layer. E_Z is the Zeeman energy due to the interaction between the applied magnetic field and the magnetic moments each atomic plane. The angle of the applied magnetic field is given by θ_H. In all my calculations, θ_H set the x-axis and was therefore equal to zero.

To calculate $M(H)$ we first had to determine the magnetization angle of each sublayer within the FM layers as a function of the applied magnetic field, H. This was done by minimizing Equation 3.26 with respect to the set of θ_i, $\frac{\partial E_{mag}}{\partial \theta_i}$. For a given field, H_j, the total magnetization of the FM/NM/FM structure along the direction of the applied field is:

$$M_j = \sum_{i=1}^{2N}\cos(\theta_i - \theta_H). \tag{3.27}$$

The experimental data are fit by repeating this energy minimization for different sets of A_{ex} and J_{RKKY}. The M_s of the ferromagnets was determined by high field magnetization measurements and was therefore not a fit parameter. A_{ex} and J_{RKKY} were determined to be the values that minimized the difference between the calculated and measured data, known as χ^2, is given by [49]:

$$\chi^2 = \sum_j \frac{(M_j - M_{expt\,j})^2}{\sigma_j^2}, \tag{3.28}$$

where $M_{expt\,j}$ and M_j are the measured and calculated magnetizations for the list of applied magnetic fields H_j, and σ_j is the uncertainty in the measured magnetization, M_j. All the

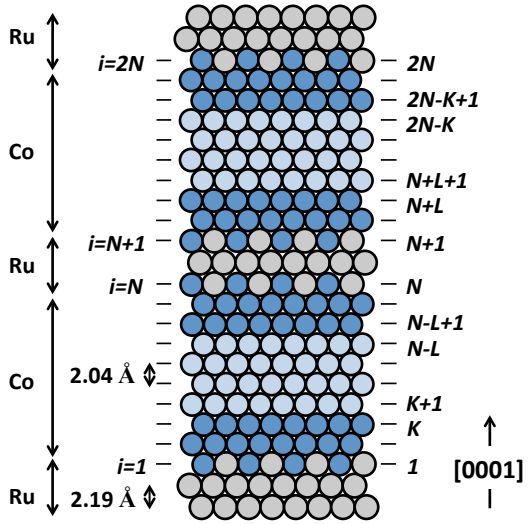

Figure 3.5: Atomistic cartoon of the seed layer (Ru)/ FM (Co)/ NM spacer layer (Ru)/ FM (Co)/ cap layer (Ru) structure used to measure A_{ex}. The atomic planes of the FM are labeled with an index i. The magnetic properties of the exterior and interior interfaces of the FM layers are changed due to the presence of the interface with non-magnetic layers. We assumed that the magnetic properties of atomic planes in the middle of the FM layer are the same as those of the bulk FM material.

coding and calculations were performed in Mathematica.

The sputter system used to grow the films did not allow for the control of atomic layer by layer growth. Thus, alloying across at least one atomic layer at the interface between Co and Ru was expected. This affects both M_s and A_{ex} at the interface of the magnetic layers. Figure 3.5 shows a cartoon of an atomistic Ru/Co/Ru/Co/Ru structure with intermixing between Co and Ru at the exterior and interior interfaces of the Co layers. A more accurate micromagnetic model would have to account for a continuous change of both M_s and A_{ex} at these interfaces. In the first approximation, I assumed that each interface layer one value of M_s and A_{ex}İ call this approximation the triple layer model, the Hamiltionian for which is:

Triple Layer Model

$$
\begin{aligned}
E &= E_{RKKY} - E_{ex} - E_Z \\
E_{RKKY} &= J_{RKKY}\cos(\theta_N - \theta_{N+1}) \\
E_{ex1} &= \frac{2A_{exint}}{d}\left[\sum_{i=1}^{K-1}\cos(\theta_i-\theta_{i+1}) + \sum_{i=2N-K+1}^{2N-1}\cos(\theta_i-\theta_{i+1})\right] \\
E_{ex12} &= \frac{2A_{exintbulk}}{d}\left[\cos(\theta_K-\theta_{K+1}) + \cos(\theta_{2N-K}-\theta_{2N-K+1})\right] \\
E_{ex2} &= \frac{2A_{exbulk}}{d}\left[\sum_{i=K+1}^{N-L-1}\cos(\theta_i-\theta_{i+1}) + \sum_{i=N+L+1}^{2N-K-1}\cos(\theta_i-\theta_{i+1})\right] \\
E_{ex23} &= \frac{2A_{expinbulk}}{d}\left[\cos(\theta_{N-L}-\theta_{N-L+1}) + \cos(\theta_{N+L}-\theta_{N+L+1})\right] \\
E_{ex3} &= \frac{2A_{expin}}{d}\left[\sum_{i=N-L+1}^{N-1}\cos(\theta_i-\theta_{i+1}) + \sum_{i=N+1}^{N+L-1}\cos(\theta_i-\theta_{i+1})\right] \\
E_{Z1} &= M_{sint}Hd\left[\sum_{i=1}^{K}\cos(\theta_i-\theta_H) + \sum_{i=2N-K+1}^{2N}\cos(\theta_i-\theta_H)\right] \\
E_{Z2} &= M_{sbulk}Hd\left[\sum_{i=K+1}^{N-L}\cos(\theta_i-\theta_H) + \sum_{i=N+L+1}^{2N-K}\cos(\theta_i-\theta_H)\right] \\
E_{Z3} &= M_{spin}Hd\left[\sum_{i=N-L+1}^{N}\cos(\theta_i-\theta_H) + \sum_{i=N+1}^{N+L}\cos(\theta_i-\theta_H)\right]
\end{aligned}
\tag{3.29}
$$

In Equation 3.29 both the direct exchange interaction and Zeeman terms are expanded to account for the different magnetic properties of the FM atomic planes at the interfaces. The exterior interfaces are the atomic planes that border the seed and capping layer while the interior interfaces are the atomic planes surrounding the Ru spacer layer, this is shown in Figure 3.5. A_{exint} is the exchange stiffness of the exterior interfaces, A_{exbulk} is the bulk exchange stiffness of atomic planes away from the interfaces, and A_{expin} is the exchange stiffness at the interior interfaces. The exchange stiffnesses at the transition between interface and bulk atomic planes is $A_{exintbulk}$ and $A_{expinbulk}$. M_{sint} is the saturation magnetization of the exterior interface, M_{sbulk} is that of the bulk, and M_{spin} is for the interior interface.

The exchange stiffness of the CoX films was calculated by fitting $M(H)$ data of CoX/Ru/CoX to the simple single layer model described by Equation 3.26. The addi-

tion of more than 10 atomic % of Ru significantly reduced the RKKY coupling between the two layers making these structures very difficult to model. A set of Ru samples were grown with an additional Co interface layer deposited around the spacer layer to increase the coupling. These $Co_{100-x}Ru_x$/Co/Ru/Co/$Co_{100-x}Ru_x$ structures were fit using the triple layer model based of Equation 3.29, where the interior interface was Co and the exterior interfaces were ignored ($A_{ex\,int}$=$A_{ex\,bulk}$ and $M_{s\,int}$=$M_{s\,bulk}$).

The dependence of the exchange stiffness on Co layer thickness in Co/Ru/Co film structures was also investigated. For thick Co layers the single layer model can be used to accurately estimate exchange stiffness, because the majority contribution is from bulk atomic planes. In thinner films the bulk contribution to the average exchange stiffness decreases thereby making the interface contribution more prominent.

The single layer micromagnetic model, Equation 3.26, produced an average value of the exchange stiffness within the magnetic layer. I used this model to fit measured $M(H)$ data obtained for Co/Ru/Co, where Co thickness ranged from 24 Å to 200 Å. The results showed very weak thickness dependence of A_{ex} for Co layers thicker than 80 Å. For this reason I used the single layer model to fit $M(H)$ data for CoX/Ru/CoX structures with CoX thickness larger or equal 100 Å and measure the bulk values of M_s and A_{ex} for CoX. These M_s and A_{ex} values were then used in the triple layer model, Equation 3.29, to determine M_s and A_{ex} of Co at the interface with Ru.

Figure 3.6 shows fits to Co using the single layer model, Equation 3.26, and to $Co_{80}Ru_{20}$ data using the triple layer model, Equation 3.29. The subscript in the alloy is the elemental percentage in the alloy. To fit to the experimental $M(H)$ data, I first determined the M_s of the CoX layers from $M(H)$ data at magnetic fields above 30 kOe. At these fields I assumed that the magnetization is fully saturated. The model confirmed that the magnetization of CoX/Ru/CoX structures should fully saturate above 30 kOe for Co alloys with X concentration below or equal to 10 atomic %. Only in CoRu/Co/Ru/Co/CoRu structures with Ru concentration above 10 atomic % did larger fields have to be applied in order to fully saturate the magnetization along the field direction. For these structures M_s was extracted from fields above 45 kOe. The SQUID magnetometer used for these measurements was limited to fields below 50 kOe. Figure 3.7 shows both the calculated and measured $M(H)$ curves of Co/Ru/Co and the difference between the two curves, known as the residuals.

I used the following fitting procedure to calculate A_{ex}. First, I found A_{ex} and J_{RKKY}

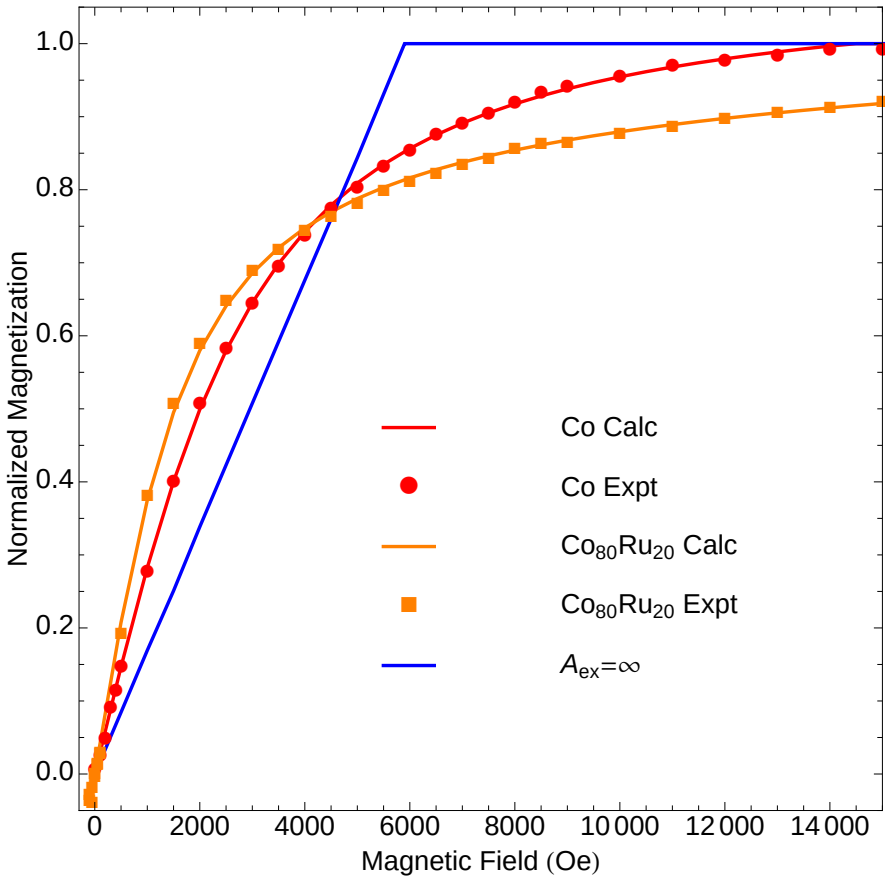

Figure 3.6: Fits to $M(H)$ data of Co/Ru/Co using the single layer micromagnetic model and fits to $M(H)$ data of $Co_{80}Ru_{20}$/Co/Ru/Co/$Co_{80}Ru_{20}$ using a double layer micromagnetic model. In both FM/NM/FM structures the total thickness of FM layers is 10 Å. The solid blue line represents the calculated $M(H)$ curve of a sample with infinite stiffness.

values that gave a good visual fit to the experimental data and used these as initial guesses. Then I determined χ^2 for a grid of A_{ex} and J_{RKKY} values around these initial values. In this thesis, we reported the values with the lowest χ^2. An example χ^2 plot for Co(100 Å)/Ru/Co(100 Å) is shown as a function of A_{ex} and J_{RKKY} in Figure 3.8.

The quality of the fit is determined by the magnitude of χ^2. A perfect fit has a χ^2 equal to zero but a fit to within the 1σ has a χ^2 equal to the number of data points. Figure 3.8 shows the 1σ, 2σ, and 3σ confidence intervals in A_{ex} and J_{RKKY} from the fitting of Co(100 Å)/Ru/Co(100 Å). The 1σ confidence interval is determined from the region satis-

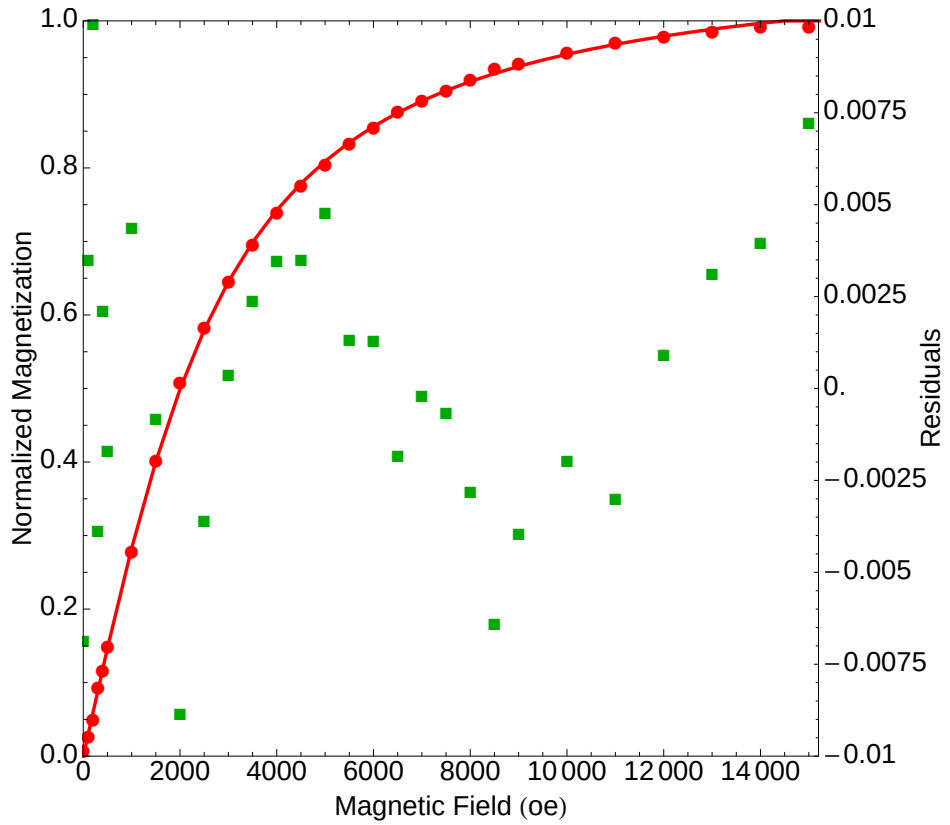

Figure 3.7: The quality of the fit to the measured $M(H)$ data was determined by minimizing the residuals, the difference between the calculated and measured values of the magnetization. This figure presents both calculated and measured $M(H)$ curves of Co/Ru/Co using the single layer micromagnetic model and fits. The filled red circles are the measured values while the line is the fitted curve. The filled green squares are residuals from the fit.

fying the condition $\chi^2 \leq N+1$ where N is the number of points used to calculated χ^2 [49]. The 1σ error bars from Figure 3.8 are 0.03×10^{-11} J/m for A_{ex} and 0.02 mJ/m^2 for J_{RKKY}.

The J_{RKKY} and A_{ex} parameters that I used to fit $M(H)$ dependences in Figure 3.6 are: J_{RKKY} = 3.67 mJ/m^2 and A_{ex}= 1.49×10^{-11} J/m for Co in Co/Ru/Co structure, and J_{RKKY} = 2.94 mJ/m^2, $A_{ex\,pin}$ = 0.5×10^{-11} J/m, and A_{ex}= 0.36×10^{-11} J/m for $Co_{80}Ru_{20}$/Co/Ru/Co/$Co_{80}Ru_{20}$. From Figure 3.6, in layers with larger A_{ex}, the magnetization of the ferromagnetic layers saturates along the field direction at lower fields than in layers with lower A_{ex}. In other words if A_{ex} is smaller, the interior interface layers expe-

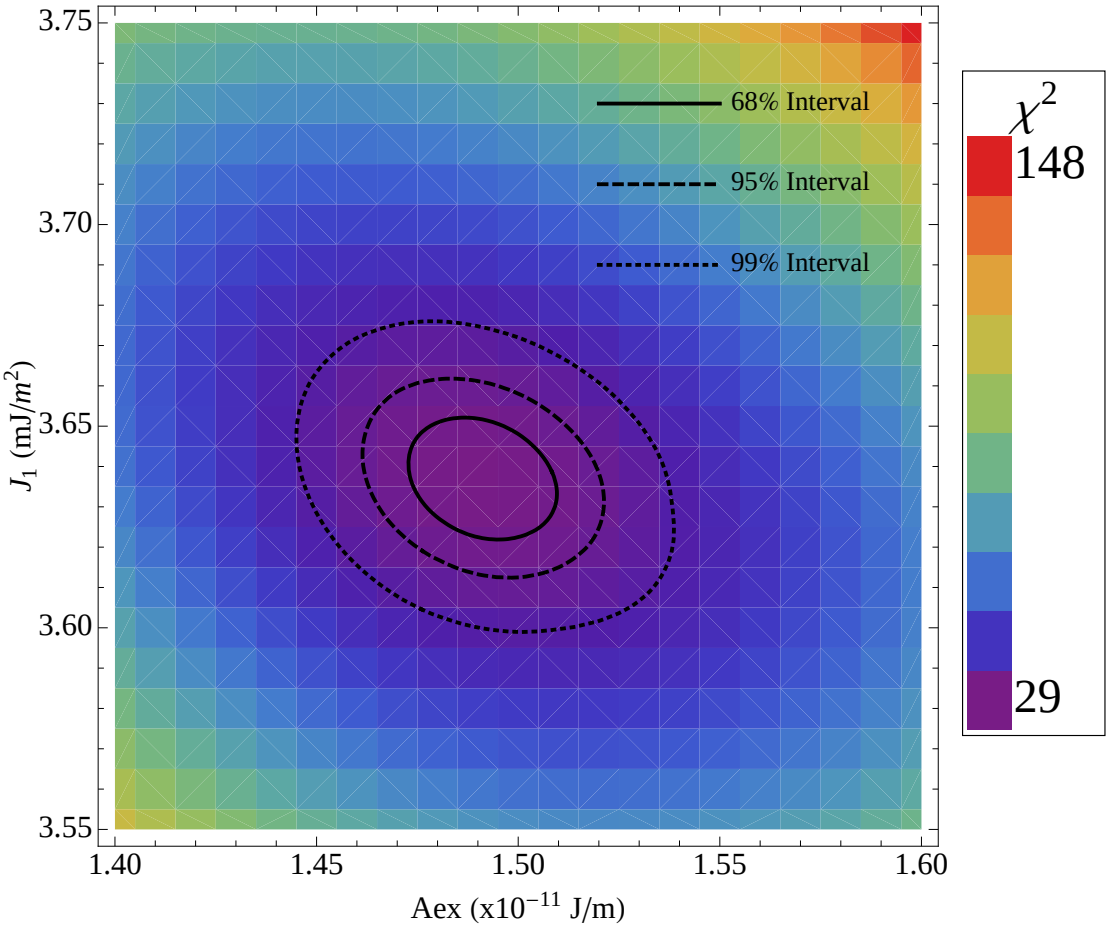

Figure 3.8: χ^2 values from fitting the $M(H)$ dependence of Co(100 Å)/Ru/Co(100 Å) for a grid of A_{ex} and J_{RKKY} values around the initial estimate. The minimum χ^2 value occurs for A_{ex}= 1.49×10^{-11} J/m and $J_{RKKY} = 3.64$ mJ/m^2. The solid line encircles the 1σ confidence interval, the dashed line the 2σ interval, and dotted line the 3σ interval.

rience less rotation forces during the reversal from the bulk and exterior layers. If A_{ex} in ferromagnetic layers is infinitely large, the $M(H)$ dependence is linear and magnetization in ferromagnetic layers saturates at the lowest field that can be calculated from the following expression:

$$H_{sat} = \frac{2J_{RKKY}}{M_s d} = 5.9kOe, \tag{3.30}$$

where J_{RKKY} = 3.67mJ/m^2 = 3.67 erg/cm^2, M_s= 1250 emu/cm^3, and Co thickness d = 100 Å.

3.3 First Principle Calculations

First principle calculations based on density functional theory, DFT, were used to predict intrinsic properties of CoRu, CoPt, and CoCr alloys and were performed by Myrasov et al. [50] at the University of Alabama. He calculated the change in the A_{ex} and M_s of Co upon the addition of Ru, Cr, and Pt. He also calculated the magnetic moments of individual atoms in these alloys. While these calculations are not part of this thesis the conclusions from these calculations were used to understand the measured and fitted trends of M_s and A_{ex}.

Chapter 4

Results

The results of this project included measurements of $M(H)$ loops from which the M_s was determined and A_{ex} and J_{RKKY} were calculated. The M_s and A_{ex} data were compared with results of DFT calculations and XMCD measurements. This chapter is divided up into three sections. In the first section I present measurements of both M_s and A_{ex} of Co as a function of Co layer thickness in Co/Ru/Co. The next section covers the primary focus of the thesis, measuring A_{ex} of CoX alloys. I chose X to be: Cr, Fe, Ni, Pd, Pt, and Ru as these elements are frequently used to modify the magnetic properties of Co. For example the addition of Pt increases the anisotropy of Co, Fe increases the M_s, Cr reduces the M_s without affecting the anisotropy, and Ru is commonly used as an interface layer for Co. Currently, these Co alloys are used for fabrication of recording media in hard drives. Co has the largest exchange stiffness of the 3d elemental ferromagnets and there is no systematic study on how alloying affects this parameter. The final section explains the effect of composition on these intrinsic magnetic parameters using DFT calculations done by Oleg Myrasov and XMCD measurements by Olof Karis.

4.1 Testing for interface effects

The exchange stiffness and saturation magnetization of a 100 Å Co film in my Ta/Cu/Ru/Co/Ru/Co/Ru multilayer structure are measurably less than the quoted values for bulk Co. I determined that for a 108 Å Co film in this structure, $A_{ex}= 1.55 \pm .09 \times 10^{-11}$ J/m and $M_s= 1250 \pm 40$ emu/cm^3. As was mentioned in the introduction, this is on the low end

of the literature values of A_{ex}: $1.8 \pm .3 \times 10^{-11}$ J/m from BLS [24], $2.7 \pm .1 \times 10^{-11}$ J/m from neutron scattering [27], and 2.1×10^{-11} J/m from FMR studies [28]. In addition to having larger values of A_{ex} these groups also have larger values for $M_s$compared with my samples: 1325 ± 50 emu/cm^3 [24], 1450 emu/cm^3 [27].

In my thin film structures a large fraction of the Co atoms share an interface with Ru atoms. This is expected to change the magnetic properties of (these) thin film Co layers. This could explain the reduced values of A_{ex} and M_s compared to those of Co bulk or of Co thick films reported in the literature. I measured $M(H)$ of twenty four Ta/Cu/Ru/Co/Ru/Co/Ru structures where the thickness of Co films was varied from 24 Å to 200 Å and used the single layer model to determine A_{ex}. The exchange stiffness as a function of the thickness of the Co film is shown in Figure 4.1. The dashed lines on the plot show the 1σ confidence interval for the exchange stiffness of a 100 Å film. The interval was determined from the standard devation in A_{ex} of five 108 Å films added in quadrature to the 1σ interval from the χ^2 plot shown in Figure 3.8. For films thicker than 80 Å, A_{ex} remains constant, i.e., there is no measurable increase in A_{ex}. However, it is expected that A_{ex} further increases with Co film thickness due to the surface effects that become negligble at larger thicknesses. This increase appears to be rather slow and requires many more measurements in order to determine the trend.

The M_s values of these Co films do not show the same sharp decrease with the Co film thickness as found for the exchange stiffness, Figure 4.1. Every structure except that with 24 Å thick Co layers has an M_s value within 1σ of the M_s of a 108 Å Co layer. This is shown in Figure 4.2. I also measured the M_s of 800 Å thick Co layer to be 1357 emu/cm^3. This thick single layer Co film was deposited on top of 30 Å of Ta and covered with 30 Å thick Ta layer. The Ta layer was used to protect Co film from oxidation. This shows that in thick films M_s approaches Co bulk value of about 1400 emu/cm^3 [24, 25].

The presence of Ru interfaces has much a stronger effect on A_{ex} than on M_s. By reducing the thickness of Co films from 100 Å to 30 Å in Ta/Cu/Ru/Co/Ru/Co/Ru structures A_{ex} is reduced to half while M_s remains practically unchanged. If M_s is also reduced with the thickness of Co films one could argue that this may be due to a systematic error in measuring Co thickness. Thus, these results clearly indicate that A_{ex} is reduced at the Co/Ru interfaces.

In order to determine whether the interface layers had a different exchange stiffness

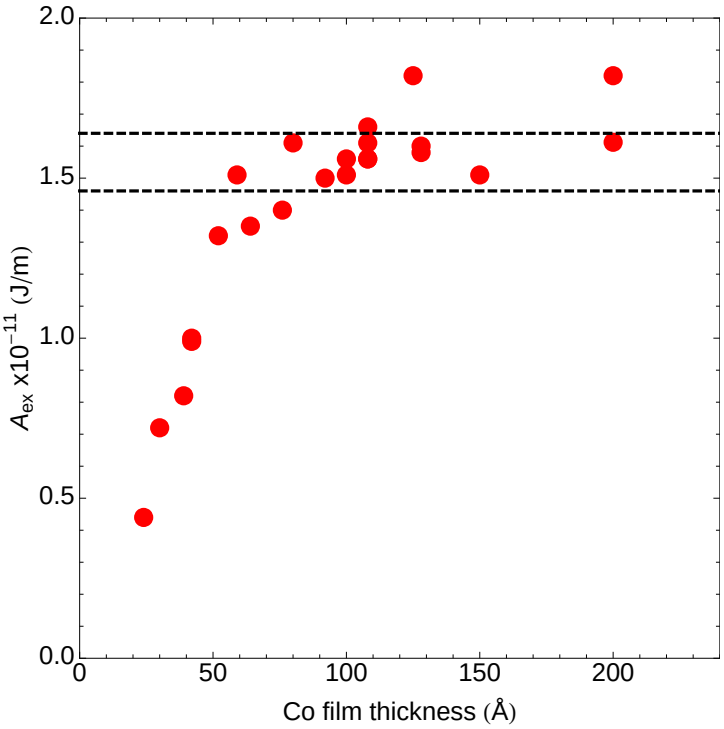

Figure 4.1: The exchange stiffness of the Co films in Ta/Cu/Ru/Co/Ru/Co/Ru structures as a function of the film thickness. The exchange stiffness is constant in Co films thicker than 80 Å but drops sharply at lower film thicknesses. This is due to a reduction in A_{ex} at the Co/Ru interfaces. The dashed black lines represent the 1σ interval for the exchange stiffness of the 100 Å Co film.

compared to the middle layers (see Figure 3.5), I fit a 100 Å thick Co/Ru/Co structure using the three layer model from Equation 3.29. For these fits I set the exchange stiffness of the interior interface, $A_{ex\,pin}$, and the exterior interface, $A_{ex\,int}$, and determined the values of the bulk stiffness and the RKKY coupling that minimized χ^2. I ran 16 different minimizations where $A_{ex\,pin}$ was 1.5×10^{-11} J/m, 1.0×10^{-11} J/m, 0.5×10^{-11} J/m, 0.25×10^{-11} J/m, and for each of these values $A_{ex\,int}$ was 1.5×10^{-11} J/m, 1.0×10^{-11} J/m, 0.5×10^{-11} J/m, 0.25×10^{-11} J/m. The interface layers were assumed to be 12 Å thick with an M_s of 1080 emu/cm^3. This M_s value was taken from the thinnest sample that I measured, Ru/Co(24 Å)/Ru/Co(24 Å)/Ru.

Figure 4.3 shows the optimal bulk exchange stiffness values when $A_{ex\,pin} = 1.5 \times 10^{-11}$

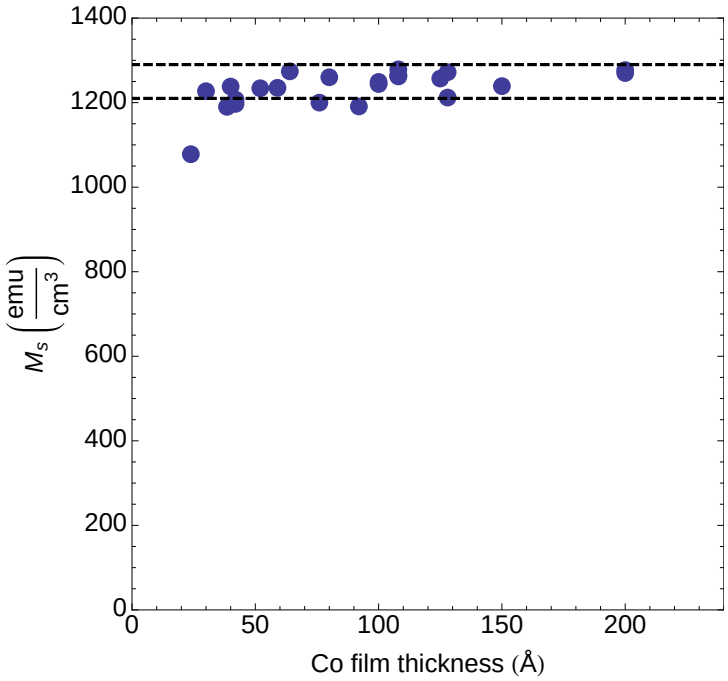

Figure 4.2: The magnetization saturation of the Co films in Ta/Cu/Ru/Co/Ru/Co/Ru structures as a function of the Co film thickness. The reduction of M_s was observed only in the structure with the 24 Å thick Co films.

J/m and $A_{ex\,int}$ varies. In these fits, the exchange stiffness of the interior interface layer was set to the value that I calculated for Co using the single layer model in Figure 3.8. The exchange stiffness of the exterior interface has very little impact on the calculated bulk stiffness or the χ^2 value of the fit. The χ^2 values for these four fits are within the 2σ interval of the fit obtained using the single layer model shown in Figure 3.8.

While the exchange stiffness of the exterior interface does not affect the optimal fitting parameters to any great extent, Figure 4.4 establishes that the exchange stiffness of the interior interface greatly affects whether a good fit to the data can be obtained. For these calculations, the exchange stiffness of the exterior interface was kept constant, $A_{ex}\ int = 1.5 \times 10^{-11}$ J/m. As the stiffness of the interior interface is decreased, the best fits have a larger bulk layer stiffness. The quality of the fits decreases as the exchange stiffness of the interior interface layer is reduced. The difference in χ^2 for the fit with $A_{ex\,pin} = 1.5 \times 10^{-11}$ J/m and for $A_{ex\,pin} = 1.0 \times 10^{-11}$ J/m is less than 2σ. However, for lower $A_{ex\,pin}$ values the

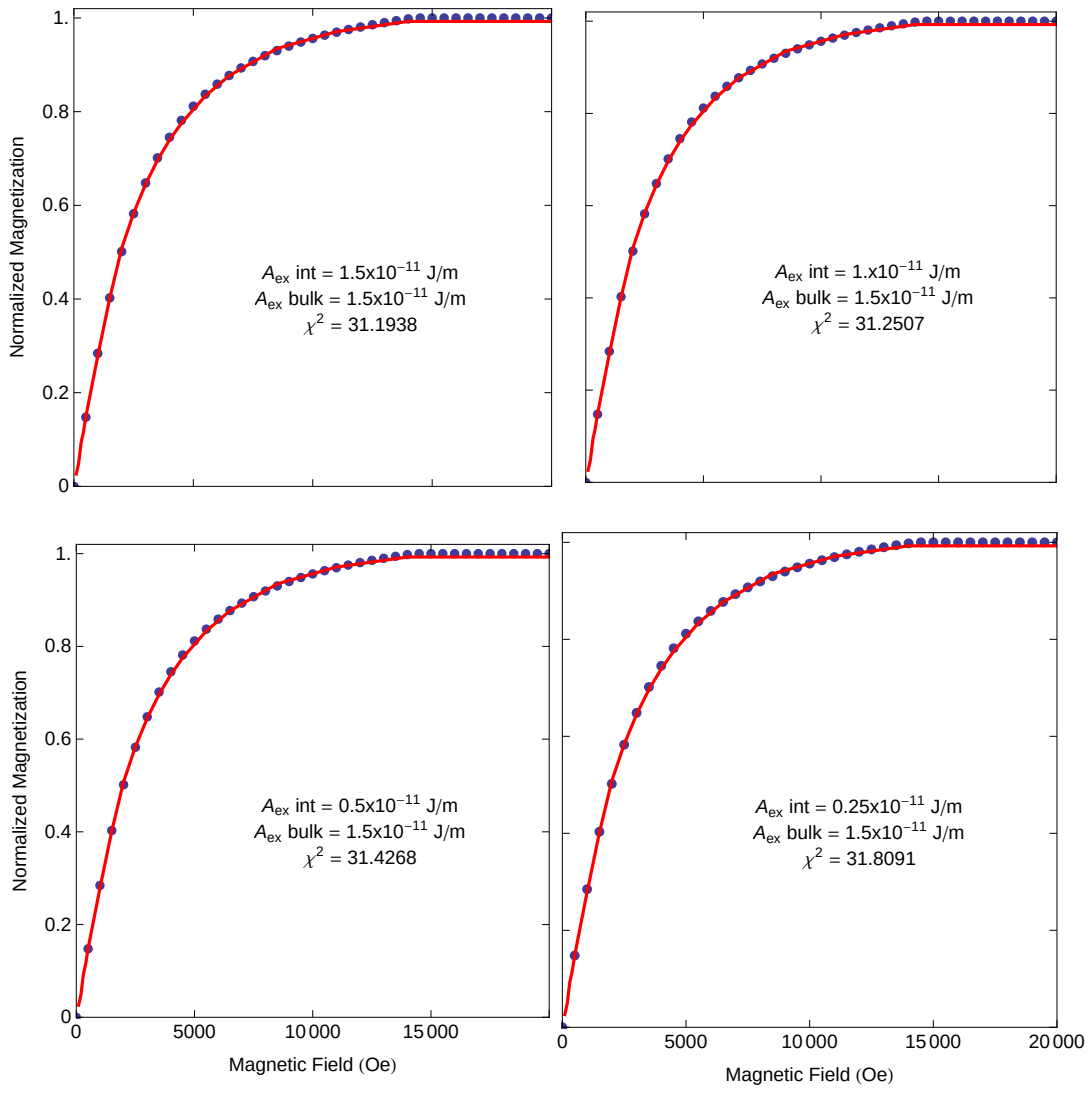

Figure 4.3: The triple layer model allows for individual adjustments of the exchange stiffness for the different layers. In this case, the exchange stiffness of the exterior interface, $A_{ex\ int}$, was varied greatly, and the best fit was determined over a grid of J_{RKKY} and $A_{ex\ bulk}$ values. In all 4 cases, the χ^2 values of the fits are within the 2σ interval for the minimum χ^2 calculated from the single layer model.

decrease in the quality of the fit is more pronounced. For $A_{ex\,pin} = 0.5 \times 10^{-11}$ J/m, χ^2 of the fit is ten times larger than that obtained from the fit with $A_{ex\,pin} = 1.5 \times 10^{-11}$ J/m and the χ^2 for $A_{ex\,pin} = 0.25 \times 10^{-11}$ J/m in one hundred times larger.

Therefore, I also fit the $M(H)$ of the Co(100 Å)/Ru/Co(100 Å) film structure using $A_{ex\,pin} = 1.1 \times 10^{-11}$ J/m, $A_{ex\,pin} = 1.2 \times 10^{-11}$ J/m, $A_{ex\,pin} = 1.3 \times 10^{-11}$ J/m, and $A_{ex\,pin} = 1.4 \times 10^{-11}$ J/m. In each case, I determined the minimum χ^2 value in terms of both $A_{ex\,bulk}$ and J_{RKKY}. Because Figure 4.3 showed that the exchange stiffness of the exterior interface did not significantly affect the fit, I assumed that this interface layer had the same properties as the bulk layer. These calculations are shown in Figure 4.5. When $A_{ex\,pin} = 1.3 \times 10^{-11}$ J/m and $A_{ex\,pin} = 1.4 \times 10^{-11}$ J/m the best fits have smaller χ^2 values than the best value calculated with the single layer model.

These results show that the exchange stiffness of interior interface does not decrease significantly due to the presence of a monolayer thick Ru spacer layer. Thus, the decrease in the stiffness that we observed in thin Co layers has to be due to the decrease in the stiffness of the exterior interface, $A_{ex\,int}$. This is in agreement with the results by Himi et al. [51] that experimentally showed that an increase in the thickness of the Ru spacer layer in Co/Ru/Co multilayers reduces the magnetization of the thin Co layer. If the magnetization of the Co films decrease with Ru spacer thickness, it is expected that A_{ex} of these Co films will decrease more that the M_s with increasing Ru thickness. Since the spacer layer in the investigated structures is only slightly more than one monolayer thick while the exterior Co interfaces border a 50 Å thick Ru film, reduction of A_{ex} at the exterior interfaces should be larger. These results also show that very good fits can be obtained using the single layer model. From the single layer model, I calculated that A_{ex} of Co was 1.49×10^{-11} J/m and with the triple layer model I calculated an exchange stiffness of the Co bulk layer to be between 1.5×10^{-11} and 1.8×10^{-11} J/m, depending on the exchange stiffness of the interface layers.

Figure 4.3 and Figure 4.4 are of particular interest as well because they demonstrate the sensitivity of the micromagnetic model to the properties of the interface layers. The model is unable to adequately resolve the properties of the exterior interface. This is attributable to the fact that magnetization reversal in the exterior interfaces depends on the reversal in the bulk and interface layers. On the other hand, the model is particularly responsive to changes in the exchange stiffness of the interior interface because these layers control

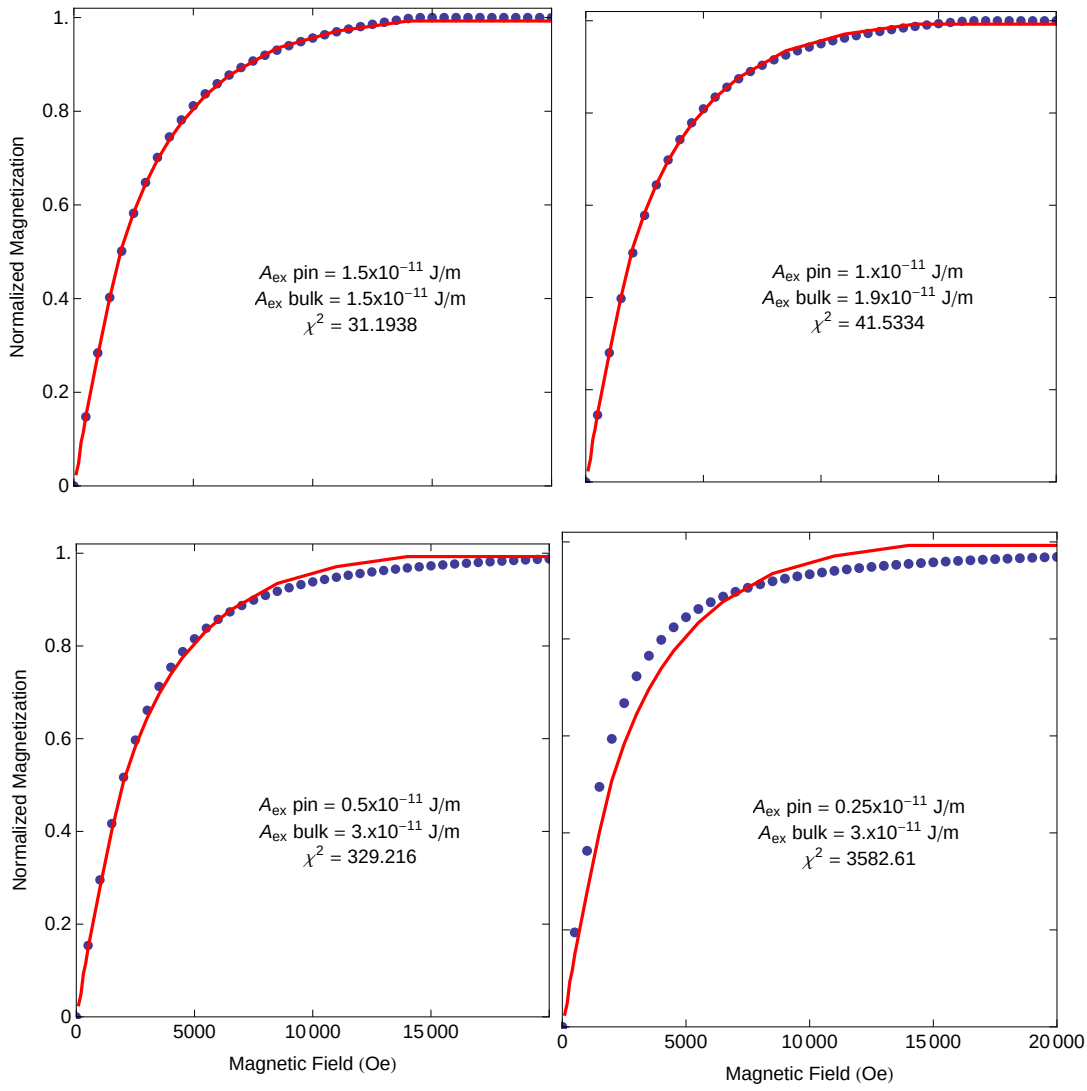

Figure 4.4: These calculated $M(H)$ curves represent the best fits to the data when A_{ex} of the interior interface layer, $A_{ex\,pin}$ is varied over a wide range. Again, the best fit is determined by calculating χ^2 for a grid of J_{RKKY} and $A_{ex\,bulk}$ values. The quality of the fits decreases dramatically as the stiffness of the interior interface layer is decreased.

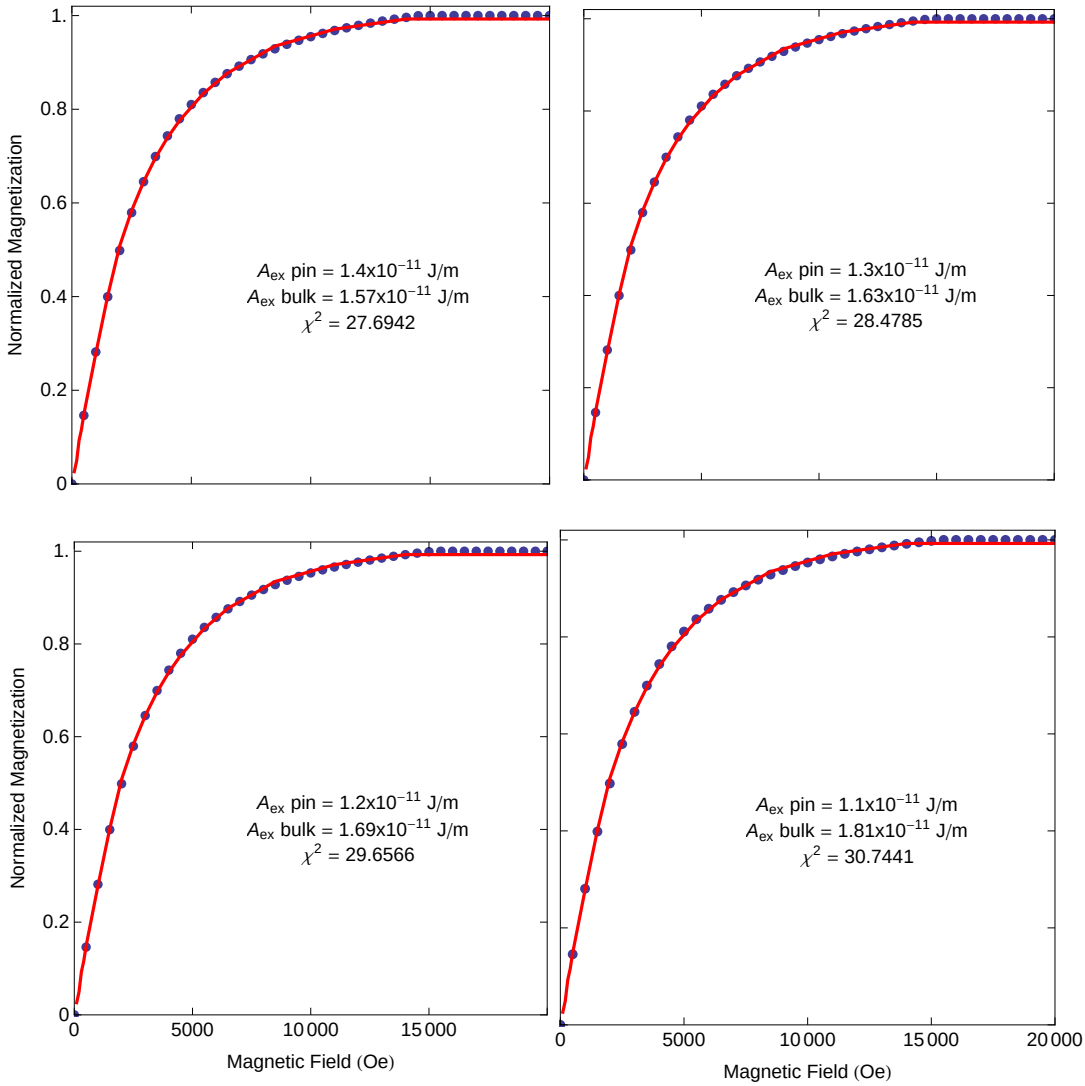

Figure 4.5: Calculated $M(H)$ curves for $A_{ex\ pin}$ values between 1.1×10^{-11} J/m and 1.4×10^{-11} J/m. All of these fits are within the 2σ χ^2 interval from Figure 3.8 anf the two fits for $A_{ex\ pin} = 1.4 \times 10^{-11}$ J/m and $A_{ex\ pin} = 1.3 \times 10^{-11}$ J/m have a smaller χ^2 value then the minimum value from Figure 3.8.

reversal of bulk and exterior interface layers.

As the two models calculated significantly different values of the exchange stiffness of Co, ranging from 1.5 to 1.8×10^{-11} J/m, the calculations of the exchange stiffness of the alloys are normalized using A_{ex} of Co= 1.55×10^{-11} J/m. The M_s values were normalized to the M_s of Co, 1250 emu/cm^3. As discussed before, these value was obtained from 5 different Co/Ru/Co structures with 108 Å thick Co layers.

4.2 Compositional effects

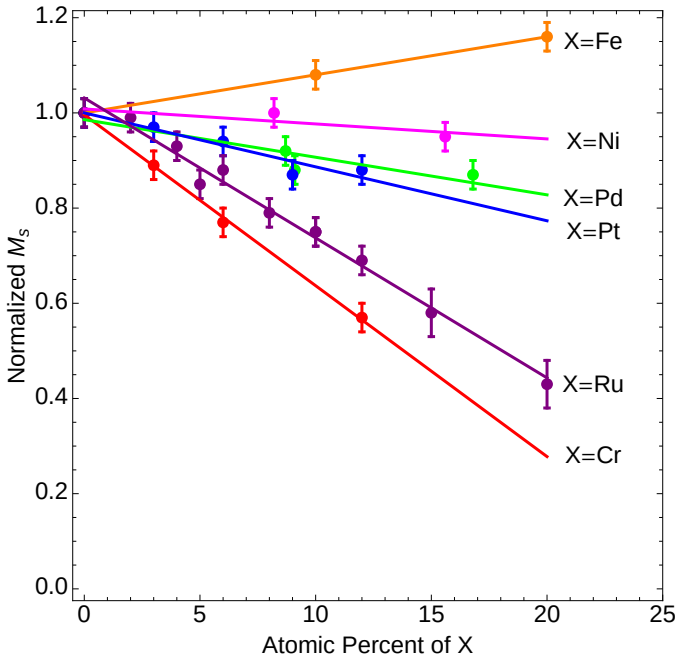

Figure 4.6: This graph summarizes the effect of alloying on the M_s of Co. The M_s values are normalized to the M_s of Co, which was 1250 ± 40 emu/cm^3 for 108 Å thick Co films. In CoX films, Cr reduces the M_s the most followed by Ru, Pt, Pd, and Ni. On the other hand, the addition of Fe increases the M_s. The lines are a linear fit through the points and are intended to help identify the M_s trends.

Figure 4.6 and Figure 4.7 show the effect that alloying has on the M_s and A_{ex} of Co in Ta/Cu/Ru/CoX(100 Å)/Ru/CoX(100 Å)/Ru, where X = Cr, Fe, Ni, Ru, Pd, and Pt. For most

of the CoX compositions we deposited two samples, one with 3.3 and other with 3.8 Å thick Ru spacer layers. So the reported values are an average of the two measurements. From only two measurements the error bars can not be accurately estimated. For this reason, for all data in Figure 4.6 and Figure 4.7 I used the larger error bars of two: one obtained for pure Co layers (where I measured 5 different samples of the same thickness), and second obtained for CoX layers (where I had only two measurements for the same thickness and composition). Moreover the error bars for M_s and A_{ex} of CoX are larger than those for Co due to additional uncertainty in the composition.

The addition of the 12 Å Co interior interface layers in CoRu/Co/Ru/Co/CoRu structures further increases the uncertainty in the M_s and A_{ex} measurements for CoRu layers with 15 and 20 atomic % of Ru. This is due to the uncertainty in A_{ex} and M_s of the Co interface layers. I fit the CoRu/Co/Ru/Co/CoRu data assuming three different A_{ex} and M_s values of Co interface layers: A_{ex} and M_s values of 1) Pure Co, 2) $Co_{95}Ru_5$ and 3) $Co_{90}Ru_{10}$. The presented data show the average values for both M_s and A_{ex} and the error bars account for the variation in these results.

The M_s of Co is reduced by approximately 3.7% per atomic percent of Cr added, 2.5% per atomic % of Ru, 1.1% per atomic % of Pd or Pt and 0.6% per atomic % of Ni. The addition of Fe increases the M_s by about .8% per atomic % of Fe in Co.

Figure 4.7 shows that per atomic % added, A_{ex} is reduced by 5.6% for X=Ru, 3.5% for X=Cr, 2.1% for X=Pd, 1.5% for X=Ni, 1.1% for X=Pt, with no change for X=Fe. I determined from Figure 4.6 and Figure 4.7 that the rate of change of A_{ex} and M_s are not necessarily correlated. Substitutions of Cr into Co reduces M_s the most while Ru additions have the largest effect on A_{ex}. While both Ni and Fe are ferromagnetic elements, they affect these parameters in very different ways. This reflects the difference in the occupation of the 3d band that leads to different magnetic moments for these elements. The two noble metal alloys, Pt and Pd, have very similar effects on A_{ex} and M_s.

As mentioned before, Figure 4.6 and Figure 4.7 summarize the results from two structures: $Co_{(1-y)}X_y$/Ru/$Co_{(1-y)}X_y$ and $Co_{(1-y)}X_y$/Co/Ru/Co/$Co_{(1-y)}X_y$. The only difference between the two is that the latter structure has 10 Å thick Co interface layers between the CoRu and Ru layers. The former structure was used for all CoCr, CoFe, CoNi, CoPd, and CoPt alloys and some CoRu alloys. Both structures were used to determine the properties of the CoRu alloys. The additional Co layer was added only to the CoRu alloy structures

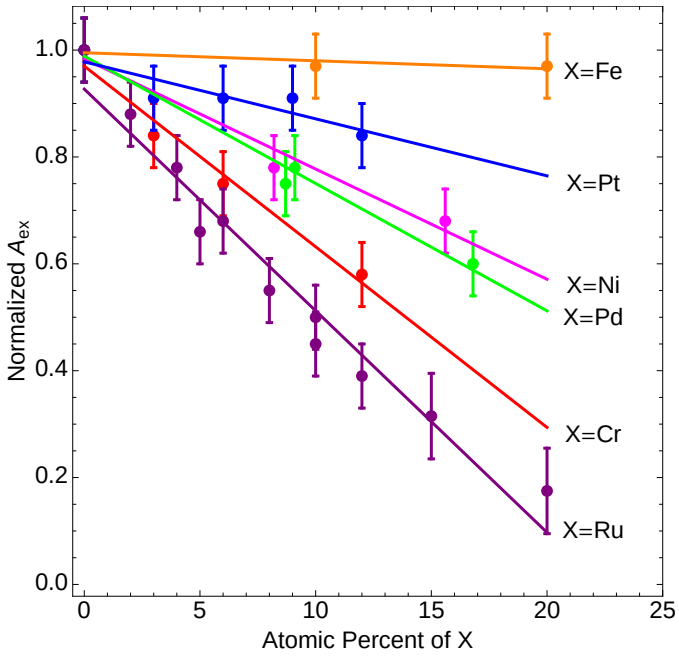

Figure 4.7: Alloying also has a strong effect on A_{ex} in Co as shown here. Again, the values are normalized to A_{ex} of pure Co, measured to be $1.55 \pm .08 \times 10^{-11}$ J/m. Alloying Co with Ru reduces A_{ex} the most followed by Cr, Pd, Ni, Pt, and then Fe. At the compositions measured, the addition of Fe has no effect on A_{ex} of Co.

to improve the RKKY coupling which dropped significantly at higher Ru concentrations. I deposited a set of CoRu alloys with 5%, 10%, 15%, and 20% of Ru with the additional 12 Å Co layer.

As is the case with calculating the stiffness of the proposed interface layers in Co/Ru/Co trilayers, determining the exact parameters for the added Co layer is quite difficult. Therefore, I did three fits for the CoX/Co/Ru/Co/CoX structures where I estimated that A_{ex} and M_s of the added Co layers are the same as Co, $Co_{95}Ru_5$, and $Co_{90}Ru_{10}$. The presented data are an average of these three fits and the error bars are slightly larger to account for this.

As expected J_{RKKY} dependence on ${M_s}^2$ is linear in CoX/Ru/CoX films for a constant Ru spacer layer thickness. The J_{RKKY} vs ${M_s}^2$ data are shown in Figure 4.8 together with a solid line representing a straight line fit through the data. In all CoX/Ru/CoX structures Ru thickness was 3.3 Å to maximize the strength of RKKY coupling.

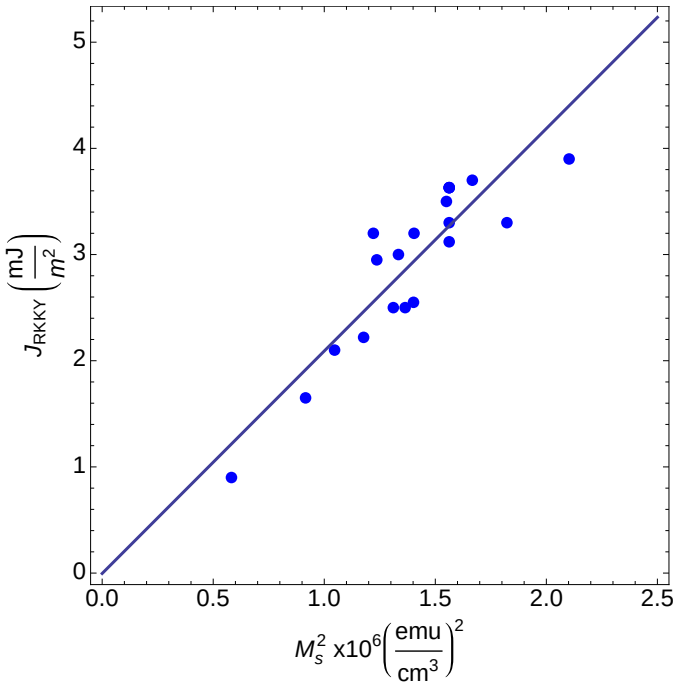

Figure 4.8: This plot shows the RKKY coupling is proportional to $M_s{}^2$. This result is in agreement with Equation 3.20.

4.3 DFT and XMCD results

The DFT calculations match much better with the experimental values of M_s, shown in Figure 4.9b, as opposed to A_{ex}, presented in Figure 4.9a. Despite this, the calculated values for A_{ex} confirm the trends observed from experiments. Of the three elements studied by DFT, Ru reduces A_{ex} the most followed by Cr then Pt. The theory confirms that the M_s of Co is reduced most strongly by Cr, then Ru, then Pt. The DFT calculations were performed at 0 K while the experimental measurements were carried out at room temperature. Preliminary results from low temperature experiments suggest that the observed difference is in part due to this temperature difference.

The effect that alloying has on M_s and A_{ex} can be explained from the results of the DFT measurements as well as XMCD measurements. The results of the DFT calculations are summarized in Table 4.1 while the XMCD measurements that confirm the DFT predictions are in Table 4.2. To calculate the effects of alloying, a Co atom in a Co lattice is replaced

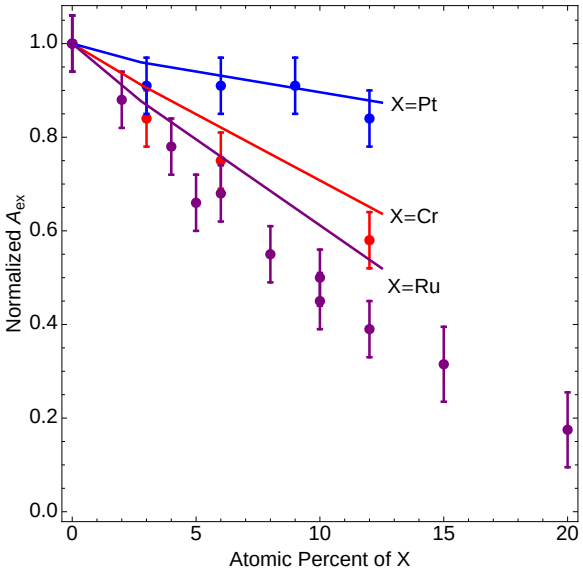

(a) Experimental and DFT calculated values of A_{ex} for CoRu, CoCr, and CoPt alloys.

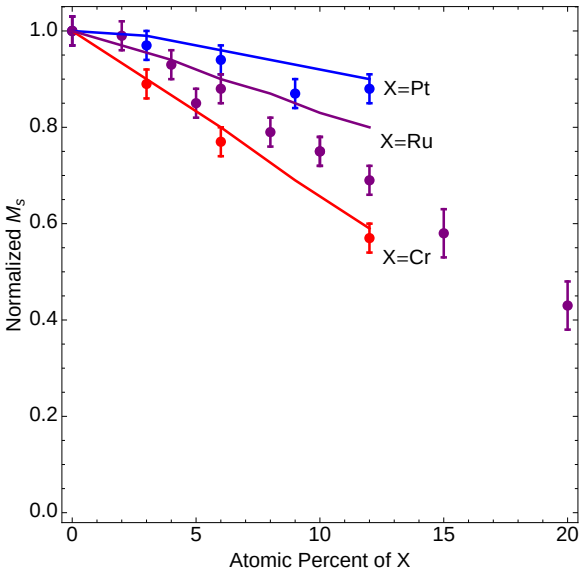

(b) M_s values for CoRu, CoCr, and CoPt obtained by experiment and DFT calculations.

Figure 4.9: DFT calculations and experimental values of A_{ex} and M_s in CoX alloys, where X is Cr, Pt and Ru.

by atom X, this atom is located at the 0 shell. The magnetic moments and direct exchange coupling of the first three sets of nearest neighbours are calculated before and after substituting an atom X for a Co atom. The nearest neighbours are in shell 1, the next nearest in shell 2 and so on. The exchange stiffness was calculated from the difference in magnetic energies before and after inducing a spin spiral to the moments in the Co lattice. The spiral is similar to that which we assume is formed in CoX films of the CoX/Ru/CoX structure in the presence of applied magnetic field.

CoX	m_i shell [μ_B]				ΔJ_i shell [mRy]				ΔJ_{av}
X	0	1	2	3	0	1	2	3	
Co	1.63	1.63	1.63	1.63	0	0	0	0	0
Pt	0.39	1.67	1.66	1.67	-13	-0.6	-0.8	0.3	-0.4
Ru	0.48	1.58	1.59	1.67	-14	-3.5	-3	-0.1	-1.6
Cr	-2.2	1.45	1.47	1.6	-0.7	-2.8	-2.5	-1	-1.4

Table 4.1: The contributions of each shell to the magnetic moment and the exchange coupling are calculated in a Co lattice with and without an impurity atom X in the 0 shell. The nearest neighbours to the 0 shell are called the 1 shell and so on. The ΔJ_i is the change in the direct exchange coupling in individual shells due to the presence of an X atom in shell 0.

XMCD	$Co_{90}Cr_{10}$		$Co_{95}Ru_5$		$Co_{75}Pt_{25}$	
	m_{Co} [μ_B]	m_{Cr} [μ_B]	m_{Co} [μ_B]	m_{Ru} [μ_B]	m_{Co} [μ_B]	m_{Pt} [μ_B]
Exper.	1.41	-2.2	1.55	0.2	1.64	0.26
DFT calc.	1.45	-2.2	1.58	0.48	1.67	0.39

Table 4.2: XMCD measurements allow us to measure the magnetic moments of particular elements in an alloy. The results of XMCD experiments match very well with the predictions from DFT calculations.

The DFT calculations show that the substituted Cr atom is anti-ferromagnetically coupled to the Co neighbours and has a very large magnetic moment of -2.2 μ_B. The substituted Pt and Ru atoms coupled ferromagnetically to the Co atoms. The induced magnetic mo-

ments in these atoms are 0.39 μ_B for Pt and 0.48 μ_B for Ru. The DFT results also show that the addition of Cr and Ru atoms reduces the magnetic moment of the surrounding Co atoms while the addition of Pt slightly increases the neighbouring Co moments. The large antiferromagnetically coupled Cr moment combined with the reduction in the magnetic moments of Co atoms in CoCr alloys explains why the addition of Cr reduces M_s more than the other elements.

The exchange stiffness in magnetic materials is calculated by adding all exchange interactions between magnetic atoms in the crystal. The exchange coupling between two magnetic atoms can be understood using a picture of atomic magnetic moments (m_i, m_j) on sites i, j and overlapping wave functions. This picture leads to the notion of a response function $R_{ij}(x)$ that contributes to the overall exchange coupling constant between sites i and j as: $J_{ij} \sim m_i R_{ij} m_j$. Thus, according to this general description, dopant atoms will alter the exchange coupling constants via two major mechanisms: (i) variation of atomic magnetic moment and (ii) variation of response function.

The trends in A_{ex} can be qualitatively understood from the change in the magnetic moments as a result of the alloying. The small moment attributed to the Ru atom combined with the reduction in the moment of its Co neighbours amounts to a significant decrease in the overall exchange coupling constant. While Cr reduces the neighbouring moments more than Ru, this is mitigated by the very large moment on the Cr atom which acts to increase the exchange constant. Qualitatively, it is difficult to say which of these two elements reduces A_{ex} more. Pt substitutions have a very small moment and increase the moment of the Co neighbours and therefore would affect A_{ex} the least. These conclusions match the measured trends.

The addition of Ru induces the greatest change in the exchange coupling in the 0, 1, and 2 shells followed by Cr then Pt. The calculation of the exchange stiffness includes all the atomic pairs so all the ΔJ_i values are taken into account. A_{ex} is directly related to the coupling, J, so any change in J is reflected in A_{ex}.

Chapter 5

Conclusion

The exchange stiffness is one of the key parameters that controls magnetization reversal. However, it is very difficult to measure, especially in thin films. Most experiments measure A_{ex} from the dispersion curve of spin waves in ferromagnetic materials. In 100 Å thick Co films, the lowest energy magnons can be excited by 580 GHz electromagnetic waves. This frequency can not be produced by FMR and can not be detected using BLS, limiting these methods to much thicker films. I developed a micromagnetic model that calculates A_{ex} by fitting to the $M(H)$ curve of a FM/NM/FM structure.

I used sputter deposition to grow a series of Ta/Cu/Ru/CoX/Ru/CoX/Ru films where X was one of: Cr, Fe, Ni, Pd, Pt, or Ru. These films were highly textured with the [0001] axis oriented perpendicular to the surface. As a result, the uniaxial anisotropy did not affect reversal in the films. Using the model, I calculated that A_{ex} of Co is reduced by 5.6% per atomic % Ru, 3.5% per atomic % Cr, 2.1% per atomic % Pd, 1.5% per atomic % Ni, 1.1% per atomic % Pt. There was no measured change to A_{ex} when Fe was added to Co. In addition, the M_s of CoX is reduced by approximately 3.7% per atomic % Cr, 2.5% per atomic % Ru, 1.1% per atomic % Pd, per atomic % Pt, and 0.6% per atomic % Ni. The addition of Fe increases the M_s by about .8% per atomic % Fe.

DFT calculations performed by Oleg Myrasov on CoCr, CoPt, and CoRu alloys agree with the trends in M_s and A_{ex} from the micromagnetic model. XMCD measurements done by Olof Karis of the magnetic moments of the individual elements in these alloys agreed with the DFT predictions. The DFT calculations were performed at 0 K while the experimental measurements were done at room temperature. Initial $M(H)$ measurements on

CoRu/Co/Ru/Co/CoRu performed at 10 K are in better agreement with the DFT calculations. This suggests that the discrepancy between the calculated and experimental M_s and A_{ex} data is in part due to this temperature effects.

These alloys are of particular interest to the recording industry as they are used in current storage media. There is also significant interest in these alloys for spin-torque-transfer magnetic random access memory. Knowledge of the magnetic parameters will allow for tailoring of the media to match the application.

Bibliography

[1] E. Girt, W. Huttema, O. N. Mryasov, E. Montoya, B. Kardasz, C. Eyrich, B. Heinrich, A. Y. Dobin, and O. Karis. A method for measuring exchange stiffness in ferromagnetic films. *J. Appl. Phys.*, 109(7):07B765, 2011.

[2] S. N. Piramanayagam. Perpendicular recording media for hard disk drives. *J. Appl. Phys.*, 102:011301, 2007.

[3] E. Grochowski and R. F. Hoyt. Future trends in hard disk drives. *IEEE Trans. Magn.*, 32(3):1850, 1996.

[4] R. Wood. Future hard disk drive systems. *J. Magn. Magn. Mater.*, 321:555, 2009.

[5] A. Moser, K. Takano, D. T. Margulies, M. Albrecht, Y. Sonobe, Y. Ikeda, S. Sun, and E. E. Fullerton. Magnetic recording: advancing into the future. *J. Phys. D: Appl. Phys.*, 35:R157, 2002.

[6] R. E. Rottmayer, S. Batra, D. Buechel, W. A. Challener, J. Hohlfeld, Y. Kubota, L. Li, B. Lu, C. Mihalcea, K. Mountfield, K. Pelhos, C. Peng, T. Rausch, M. A. Seigler, D. Weller, and X. Yang. Heat-assisted magnetic recording. *IEEE Trans. Magn.*, 42 (10):2417, 2006.

[7] J. A. Katine and E. E. Fullerton. Device implications of spin-transfer torques. *J. Magn. Magn. Mater.*, 320:1217, 2008.

[8] S. Mangin, D. Ravelosona, J. Katine, M. J. Carey, B. D. Terris, and E. E. Fullerton. Current-induced magnetization reversal in nanopillars with perpendicular anisotropy. *Nat. Mat.*, 5:210, 2006.

[9] K. Nagasaka. Cpp-gmr technology for magnetic read heads of future high-density recording systems. *J. Magn. Magn. Mater.*, 321:508, 2009.

[10] S. Thompson. The discovery, development and future of gmr: the nobel prize 2007. *J. Phys. D: Appl. Phys.*, 41:2008, 2008.

[11] J. Lenz and A. S. Edelstein. Magnetic sensors and their applications. *IEEE Sensors J.*, 6(3):631, 2006.

[12] E. E. Fullerton, D. T. Margulies, M. E. Schabes, M. Carey, B. Gurney, A. Moser, M. Best, G. Zeltzer, K. Rubin, H. Rosen, and M. Doerner. Antiferromagnetically coupled magnetic media layers for thermally stable high-density recording. *Appl. Phys. Lett.*, 77(23):3806, 2000.

[13] J. W. Lau and J. M. Shaw. Magnetic nanostructures for advanced technologies: fabrication, metrology and challenges. *J. Phys. D: Appl. Phys.*, 44:303001, 2011.

[14] Y. Shiroishi, K. Fukuda, I. Tagawa, H. Iwasaki, S. Takenoiri, H. Tanaka, H. Mutoh, and N. Yoshikawa. Future options for hdd storage. *IEEE Trans. Magn.*, 45(10):3816, 2009.

[15] C. A. Ross. Patterned magnetic recording media. *Annu. Rev. Mater. Res.*, 31:203, 2001.

[16] T. W. McDaniel, W. A. Challener, and K. Sendur. Issues in heat-assisted perpendicular recording. *IEEE Trans. Magn.*, 39(4):1972, 2003.

[17] D. Suess, T. Schrefl, M. Kirschner, G. Hrkac, F. Dorfbauer, O. Ertl, and J. Fidler. Optimization of exchange spring perpendicular recording media. *IEEE Trans. Magn.*, 41(10):3166, 2005.

[18] D. Suess. Multilayer exchange spring media for magnetic recording. *Appl. Phys. Lett.*, 89:113105, 2006.

[19] D. Suess, J. Lee, J. Fidler, and T. Schrefl. Exchange-coupled perpendicular media. *J. Magn. Magn. Mater.*, 321:545, 2009.

[20] R. H. Victora and X. Shen. Exchange coupled composite media for perpendicular magnetic recording. *IEEE Trans. Magn.*, 41(10):2828, 2005.

[21] S. Sahoo, E. Redja, I. Tabakovic, S. C. Reimer, and M. C. Kautzky. Heat assisted magnetc recording HAMR heads including components made of Nickel alloys, 2012. US Patent, 8259540.

[22] X. Shen, M. Kapoor, R. Field, and R. H. Victora. Issues in recording exchange coupled composite media. *IEEE Trans. Magn.*, 43(2):676, 2007.

[23] J. Hamrle, O. Gaier, Seong-Gi Min, B. Hillebrands, Y. Sakuraba, , and Y. Ando. Determination of exchange constants of heusler compounds by brillouin light scattering spectroscopy: application to Co_2mnsi. *J. Phys. D: Appl. Phys.*, 42:084005, 2009.

[24] S. Vernon, S. Lindsay, and M. B. Stearns. Brillouin scattering from thermal magnons in a thin co film. *Phys. Rev. B*, 29(8):4439, 1984.

[25] X. Liu, R. Sooryakumar, C. J. Gutierrez, and G. A. Prinz. Exchange stiffness and magnetic anisotropies in bcc $Fe_{1-x}Co_x$alloys. *J. Appl. Phys.*, 75:7021, 1994.

[26] X. Liu, M. M. Steiner, R. Sooryakumar, G. A. Prinz, R. F. C. Farrow, and G. Harp. Exchange stiffness, magnetization, and spin waves in cubic and hexagonal phases of cobalt. *Phys. Rev. B*, 53:166, 1996.

[27] G. Shirane, V. J. Minkiewicz, and R. Nathans. Spin waves in 3d metals. *J. Appl. Phys.*, 39(2):383, 1968.

[28] R. Krishnan. Fmr studies in compositionally modulated co-nb and co films. *J. Magn. Magn. Mater.*, 50(2):189.

[29] B. D. Cullity and S. R. Stock. *Elements of X-ray diffraction*. Prentice Hall, New Jersey, USA, 2001.

[30] C. Kittel. *Introduction to solid state physics*. Wiley, New Jersey, USA, 1997.

[31] E. Hecht. *Optics*. Addison Wesley, California, USA, 2002.

[32] J. R. Waldram. *Superconductivity of metals and cuprates*. Institute of Physics Publishing, UK, 1996.

[33] J. Clarke and A. I. Braginski. *The SQUID handbook, Volume 1*. Wiley, Weinheim, Germany, 2004.

[34] S. S. Yasin. *Electron spin resonance in low-dimensional spin chains and metals*. PhD thesis, Institute of Physics, University of Stuttgart, 2008.

[35] T. Kebe. *SQUID-magnetometry on Fe monolayers on GaAs(001) in UHV*. PhD thesis, University of Duisberg-Essen, 2006.

[36] R. Knut. *New materials for spintronics: electronic structure and magnetism*. PhD thesis, Uppsala University, 2012.

[37] B. Kardasz. *Anisotropies and spin dynamics in ultrathin magnetic structures*. PhD thesis, Simon Fraser University, 2009.

[38] S. Chikazumi. *Physics of ferromagnetism*. Oxford University Press, USA, 2009.

[39] D. J. Griffiths. *Introduction to quantum mechanics*. Prentice Hall, New Jersey, USA, 1994.

[40] E. Girt and H. J. Richter. Antiferromagnetically coupled perpendicular recording media. *IEEE Trans. Magn.*, 39(5):2306, 2003.

[41] M. D. Stiles, B. Heinrich, and J. A. C. Bland. *Ultrathin magnetic structures III*. Springer, Germany, 2005.

[42] K. B. Hathaway, B. Heinrich, and J. A. C. Bland. *Ultrathin magnetic structures II*. Springer, Germany, 1994.

[43] P. Bruno. Theory of interlayer exchange interactions in magnetic multilayers. *J. Phys: Condens. Matter*, 11:9403, 1999.

[44] M. A. Ruderman and C. Kittel. Indirect exchange coupling of nuclear magnetic moments by conduction electrons. *Phs. Rev.*, 96(1):99, 1954.

[45] E. Šimánek and B Heinrich. Gilbert damping in magnetic multilayers. *Phys. Rev. B*, 67:144418, 2003.

[46] J. Mathon, A. Umerski, and M. Villeret. Quantum oscillations of the spin density in magnetic multilayers. *Phys. Rev. B*, 59(9):6344, 1999.

[47] D. J. Griffiths. *Introduction to electrodynamics*. Prentice Hall, New Jersey, USA, 1999.

[48] J. Brandenburg, R. Hühne, L. Schultz, and V. Neu. Domain structure of epitaxial co films with perpendicular anisotropy. *Phys. Rev. B*, 79:054429, 2009.

[49] W. H. Press, W. T. Vetterling, S. A. Teukolsky, and B. P. Flannery. *Numerical recipes in C*. Cambridge University Press, USA, 1997.

[50] O. N. Myrasov, V. A. Gubanov, and A. I. Liechtenstein. Spiral-spin-density-waves states in fcc iron: linea-muffin-tin-orbitals band-structure approach. *Phys. Rev. B*, 45 (21):330, 1992.

[51] K. Himi, K. Takanashi, S. Mitani, M. Yamaguchi, D. H. Ping, K. Hono, and H. Fujimori. Artificial modulation of magnetic structures on a monatomic layer scale in co/ru superlattices. *Appl. Phys. Lett.*, 78(10):1436, 2001.